

A Continuous and Static Water Contaminant Detection System Using RF Microwave Principles

Rafee Mahbub
Marquette University

Recommended Citation

Mahbub, Rafee, "A Continuous and Static Water Contaminant Detection System Using RF Microwave Principles" (2019). *Master's Theses (2009 -)*. 557.
https://epublications.marquette.edu/theses_open/557

A CONTINUOUS AND STATIC WATER CONTAMINANT DETECTION SYSTEM
USING RF MICROWAVE PRINCIPLES

By

Rafee Mahbub, B.S.

A Thesis submitted to the Faculty of the Graduate School,
Marquette University,
in Partial Fulfillment of the Requirements for
the Degree of Master of Science

Milwaukee, Wisconsin

August 2019

ABSTRACT

A CONTINUOUS AND STATIC WATER CONTAMINANT DETECTION SYSTEM USING RF MICROWAVE PRINCIPLES

Rafee Mahbub, B.S.
Marquette University, 2019

A continuous, static, and non-interfering water contaminant detection method is presented to measure specific water contaminants (NaCl, MgCl₂, and mixture of NaCl and MgCl₂) using RF microwave principles. A coil is mounted on the surface of a glass tube and the liquid sample is placed inside of the tube. An external magnetic field generated by the coil continuously measures changes in radio frequency energy. The non-contact feature of the device allows a long sensor lifetime with high sensitivity for real-time measurements. The measurement parameter is reflection coefficient (S_{11}) and the operating frequency is 10 MHz – 5 GHz.

For NaCl and MgCl₂, 11 different concentrations (1000 ppm – 400 ppb) liquid solutions are prepared. Amplitude changes and frequency shifts are noticeable among different materials and concentrations. Different test materials have different radio frequencies at which they undergo excitation and the responses are identified in S_{11} measurement.

A machine learning algorithm is introduced to analyze the measured S_{11} data. A support vector regressor (SVR) model is trained using the measured data of various salt samples. The training data is constructed by concatenating the 20,000 amplitudes and 20,000 phase values from the measured S_{11} data. The hyperparameters of the SVR are optimized using 10-fold cross-validation method. Based on the trained model, the algorithm predicts the concentrations of the liquid samples. The experimental results indicate that the device can detect concentrations as low as 400 ppb with high accuracy.

ACKNOWLEDGMENTS

Rafee Mahbub, B.S.

I would like to thank my parents and sisters for their unending support, prayer, love, and guidance. I would specifically like to thank Dr. Chung Hoon Lee and Dr. James E. Richie for their time and support to guide me through my graduate career. I want to thank Dr. Henry Medeiros for his intellectual support in this project.

I would like to thank the former and current members of the Nanoscale Device Laboratory, Woojae Chung and Imtiaz Hossen for their support and assistance. I want to thank Abubakar Siddique for his support and valuable time.

I am grateful for this opportunity provided by Marquette University's Department of Electrical and Computer Engineering.

Rafee Mahbub

Milwaukee, WI

TABLE OF CONTENTS

Chapter 1	Introduction	1
1.1	Background	1
1.2	Importance of monitoring water contaminants	3
1.3	Motivation of research	5
1.4	Different methods of water contaminant detection	5
1.4.1	Ion Chromatography	6
1.4.2	Mass Spectrometry	8
1.4.3	Atomic Absorption Spectroscopy	14
1.5	Approach	16
1.6	Radio frequency signal.....	18
1.7	Thesis outline	19
Chapter 2	Principle of operation of inductive sensor	21
2.1	Inductive sensor.....	21
2.2	Inductor	21
2.3	The voltage-current relationship of an inductor	23
2.4	Equivalent circuit model of an inductor	25
2.5	Q factor.....	25
2.6	Skin effect	28

2.7	The Scattering Matrix.....	28
2.8	Forward Reflection coefficient (S_{11}).....	31
2.9	Dielectric relaxation	32
2.10	Ion responses of an AC coil.....	34
Chapter 3 Device design and measurement set-up.....		40
3.1	Device parameters	40
3.2	Inductance calculation.....	42
3.3	Self-resonance frequency calculation.....	43
3.4	Measurement set-up	45
3.5	Solution preparation for NaCl and $MgCl_2$	47
3.6	Solution preparation of NaCl and $MgCl_2$ mix	48
3.7	Vector Network Analyzer (VNA).....	49
Chapter 4 Machine learning algorithm.....		52
4.1	Introduction	52
4.2	Support vector regressor.....	53
4.3	Linear support vector machine regression model	55
4.4	Optimize SVM Regression.....	56
4.5	Flowchart of the SVR algorithm	57
4.6	Concentration prediction using support vector regressors	61
4.7	Visualization of the SVR model result.....	62

Chapter 5	Experimental Results and discussion	64
5.1	Optimization of the sensor	64
5.1.1	Optimization of the sensor for coils with different number of turns.	64
5.1.2	Optimization of the sensor with and without static magnet	69
5.2	Issues related to analyzing the reflection coefficient measurement	71
5.3	Experimental results for sodium chloride (NaCl) salt solutions	72
5.3.1	Reflection coefficient measurement.....	72
5.3.2	Machine learning approach	74
5.3.3	Standard deviation calculation for different concentrations of NaCl	77
5.3.4	Conductivity measurement for different concentrations of NaCl	80
5.4	Experimental results for magnesium chloride (MgCl ₂) salt solutions	82
5.5	Mix (NaCl and MgCl ₂) solution results	85
Chapter 6	Conclusion and Future work.....	89
6.1	Conclusion.....	89
6.2	Future work	89
Chapter 7	APPENDIX	93
7.1	Conductivity response of MgCl ₂	93
7.2	Standard deviation result for MgCl ₂	93
Bibliography	95

LIST OF TABLES

Table 1-1: Detection limit for Ion Chromatography method.....	7
Table 1-2: Frequency band designations	18
Table 3-1: Concentrations of the sample salt solutions for NaCl and MgCl ₂	48
Table 4-1: Hyperparameter optimization functions for SVR model	57
Table 5-1: Concentration prediction result after the outliers are removed from the input data sets	80

LIST OF FIGURES

Figure 1: Periodic table indicating chemical elements of interest	2
Figure 2: Working principle of Ion Chromatography method [15]	8
Figure 3: Schematic of the basic components of the Mass Spectrometer.....	11
Figure 4: Working principle of a mass spectrometer [18]	12
Figure 5: Spectrum analyzer analysis of a water sample	13
Figure 6: Working principle of Atomic Absorption Spectroscopy [20]	15
Figure 7: Typical calibration graph for Atomic Absorption Spectroscopy [21].....	16
Figure 8: Schematic drawing of the experimental set-up	18
Figure 9: Circuit symbol of an inductor.....	22
Figure 10: An inductor mounted on a glass tube	23
Figure 11: Cross-sectional view of the inductor with one turn.....	23
Figure 12: Equivalent circuit model of an inductor	25
Figure 13: (a) Series and (b) parallel LC resonant circuit	27
Figure 14: Simple transmission system [34].....	29
Figure 15: Two-port network.....	30
Figure 16: (a) Cross section of the tube (b) charge distribution across the tube (c) coordinate system.....	35
Figure 17: (a) Side view of the sensor (b) Coil structure (c) Cross-sectional view of the sensor (d) Top view of the sensor	41
Figure 18: Device structure.....	42
Figure 19: Top pictorial view of the sensor	45
Figure 20: Top pictorial view of measurement set-up (inside Faraday cage).....	46

Figure 21: Device connected with a vector network analyzer	46
Figure 22: Generalized network analyzer block diagram [34]	49
Figure 23: Vector Network Analyzer (VNA)	51
Figure 24: Machine learning classification	53
Figure 25: Soft margin loss setting for a linear support vector regressor	55
Figure 26: Flowchart of the machine learning algorithm	58
Figure 27: Phase (a) wrapped and (b) unwrapped	59
Figure 28: Min objective vs. Number of function evaluations	60
Figure 29: Prediction problem for lower concentration.....	62
Figure 30: Improved visualization with a log scale	63
Figure 31: Coils with different turns (a) 16 turns (b) 29 turns (c) 42 turns	65
Figure 32: Reflection coefficient (S_{11}) response with 16 turns coil.....	66
Figure 33: Reflection coefficient (S_{11}) response with 29 turns coil.....	66
Figure 34: Reflection coefficient (S_{11}) response with 42 turns coil.....	67
Figure 35: (a) Device holder (b) Static magnet (c) Device holder with magnet.....	70
Figure 36: Reflection coefficient S_{11} measurement without the magnets	70
Figure 37: Reflection coefficient S_{11} measurement with the magnets.....	71
Figure 38: Reflection coefficient (S_{11}) response of NaCl salt solutions for different concentrations	73
Figure 39: Reflection coefficient (S_{11}) response of NaCl salt solution for different concentrations at 413.9 MHz	74
Figure 40: Concentration prediction of NaCl salt solution (1000 ppm)	75
Figure 41: Concentration prediction of NaCl salt solution (100 ppm)	76

Figure 42: Concentration prediction of NaCl salt solution (6 ppm)	76
Figure 43: Concentration prediction of NaCl salt solution (400 ppb and 800 ppb)	77
Figure 44: Standard deviation of measured data for different concentrations of NaCl solutions	78
Figure 45: Standard deviation of measured data for different concentrations of NaCl solutions with outliers removed from red circled concentrations	79
Figure 46: Ultrameter device to measure conductivity, temperature, and pH	81
Figure 47: NaCl conductivity measurement for different concentrations of salt solution	82
Figure 48: Reflection coefficient (S_{11}) response of $MgCl_2$ salt solutions for different concentrations	83
Figure 49: Concentration prediction of $MgCl_2$ salt solution (1.5 ppm)	84
Figure 50: Concentration prediction of $MgCl_2$ salt solution (25.0 ppm)	84
Figure 51: Reflection coefficient measurement of mixed solution (NaCl+ $MgCl_2$)	85
Figure 52: Concentration prediction of mix (NaCl+ $MgCl_2$) salt solution (1.5 ppm)	86
Figure 53: Concentration prediction of mix (NaCl+ $MgCl_2$) salt solution (6 ppm)	86
Figure 54: Reflection coefficient measurement for NaCl, $MgCl_2$, and mixture solutions	87
Figure 55: NaCl (100 ppm) concentration prediction test with different concentrations of mixed train data	87
Figure 56: $MgCl_2$ (100 ppm) concentration prediction test with different concentrations of mix train data	88
Figure 57: Reflection coefficient (S_{11}) response of $Pb(NO_3)_2$ from 10 MHz – 5.0 GHz	90
Figure 58: Reflection coefficient (S_{11}) response of $Pb(NO_3)_2$ from 4.72 GHz – 4.74 GHz	91

Figure 59: Concentration prediction of $\text{Pb}(\text{NO}_3)_2$ solution (1 ppm).....	92
Figure 60: Internet of things (IoT)	92
Figure 61: MgCl_2 conductivity measurement for different concentration solutions.	93
Figure 62: Standard deviation calculation for different concentration of MgCl_2 solutions	94

CHAPTER 1 INTRODUCTION

1.1 Background

Drinking water contaminants are identified and regulated by the Environmental Protection Agency (EPA) to protect public health. The Safe Drinking Water Act (SDWA) defines the term “contaminants”. According to the act, any physical, chemical, biological, radioactive components existing in the water can be defined as “contaminants” [1]. The act refers to the contaminants as a broad subject of studies [1]. The contaminants can be classified as harmful and not harmful. Some of the contaminants show a harmful effect after consumption above a certain concentration limit. In this project, specific water contaminants have been given importance. Water quality monitoring systems started to develop in the early 1700s [2]. To achieve better quality, sand filtration was established as an effective process for removing particles in Europe during the 1800s [2]. Since then, scientists have done a series of studies, tests, and experiments and developed several water quality detection methods and purification systems.

Group I and II metals in the periodic table are known as alkali metals and alkaline earth metals respectively. In this project, sodium (Na) and Magnesium (Mg) ions are the main focus of Group I and II. Figure 1 shows the position of Na, Mg, and Cl in the periodic table. These ions are very reactive and exist as a compound in nature. In this project, sodium chloride (NaCl) and magnesium chloride (MgCl₂) salts are used as compounds of these ions.

Periodic Table of the Elements

Legend:

- Alkali Metals
- Alkaline Earth Metals
- Transition Metals
- Other Metals
- Nonmetals
- Noble Gases
- Lanthanoids
- Actinoids

Key:

element name
atomic number
symbol
atomic weight

C	Br	He	Tc
solid	liquid	gas	synthetic

hydrogen 1 H 1.00794	helium 2 He 4.002602
lithium 3 Li 6.941	beryllium 4 Be 9.012182
sodium 11 Na 22.98977	magnesium 12 Mg 24.3050
potassium 19 K 39.0983	calcium 20 Ca 40.078
rubidium 37 Rb 85.4678	strontium 38 Sr 87.62
cesium 55 Cs 132.90545	barium 56 Ba 137.327
francium 87 Fr [223]	radium 88 Ra [226]
scandium 21 Sc 44.95591	titanium 22 Ti 47.887
yttrium 39 Y 88.90585	zirconium 40 Zr 91.224
lutetium 71 Lu 174.967	hafnium 72 Hf 178.49
lanthanum 57 La 138.9055	cerium 58 Ce 140.116
praseodymium 59 Pr 140.90768	neodymium 60 Nd 144.24
promethium 61 Pm [145]	samarium 62 Sm 150.36
europium 63 Eu 151.964	gadolinium 64 Gd 157.25
terbium 65 Tb 158.9253	dysprosium 66 Dy 162.50
holmium 67 Ho 164.930	erbium 68 Er 167.259
thulium 69 Tm 168.934	ytterbium 70 Yb 173.04
actinium 89 Ac [227]	thorium 90 Th 232.038
protactinium 91 Pa 231.0369	uranium 92 U 238.0289
neptunium 93 Np [237]	plutonium 94 Pu [244]
americium 95 Am [243]	curium 96 Cm [247]
berkelium 97 Bk [247]	californium 98 Cf [251]
einsteinium 99 Es [252]	fermium 100 Fm [257]
mendelevium 101 Md [258]	nobelium 102 No [259]
boron 5 B 10.811	carbon 6 C 12.0107
aluminum 13 Al 26.981538	silicon 14 Si 28.0855
gallium 31 Ga 69.723	germanium 32 Ge 72.64
indium 49 In 114.818	tin 50 Sn 118.710
thallium 81 Tl 204.3833	lead 82 Pb 207.2
unquadrium 114 Uuq [289]	
nitrogen 7 N 14.00644	oxygen 8 O 15.9994
phosphorus 15 P 30.97376	sulphur 16 S 32.065
arsenic 33 As 74.9216	selenium 34 Se 78.96
antimony 51 Sb 121.760	tellurium 52 Te 127.60
bismuth 83 Bi 208.980	polonium 84 Po [209]
	astatine 85 At [210]
	radon 86 Rn [222]
fluorine 9 F 18.9984	chlorine 17 Cl 35.453
argon 18 Ar 39.964	krypton 36 Kr 83.798
xenon 54 Xe 131.293	radon 86 Rn [222]

Figure 1. Periodic table indicating chemical elements of interest.

Among the components in the periodic table, sodium (Na) is the sixth most abundant component on earth [3]. Due to its high soluble property, Na is found everywhere in the water system. Sodium chloride is the most important form of sodium and used in different categories, such as chemical, ice control, agriculture, food processing, general industrial, distributors, and water treatment, with an estimated 1,400 direct and indirect uses [4]. In the United States, one of the most important uses of Na is for deicing [5]. After deicing, the liquid solutions containing Na and its compounds flow through the ground and mix with other water resources. It is found that the amount of sodium salts and minerals are much larger in the groundwater than the surface water [6]. Our body takes a significant amount (1,800 to 5,000 milligrams per day) of salt in various ways [5]. Sodium chloride (NaCl) is listed as one hazardous material for drinking water

by the EPA Office of Water (OW). The maximum limit of NaCl concentration in drinking water, authorized by the EPA OW is 20mg/L [5].

1.2 Importance of monitoring water contaminants

Recent studies have shown that oral doses of high concentration of sodium chloride may cause several health-related problems, such as inflammation of the gastrointestinal tract, muscular twitching, vomiting, nausea, and convulsions [7]. Hypertension is one of the dominant health hazards due to an increase in blood pressure caused by a large intake of sodium chloride. It is required to monitor the concentration level periodically to maintain the proper amount of sodium for the treatment of people who suffer from sodium-sensitive hypertension. It is found from studies that the intake of sodium ions excessively can enhance the risk of cancer in the gastrointestinal tract [8].

The taste of sodium chloride in drinking water may vary from person to person with age and health status. The average range of the taste threshold is about 30 mg/L to 460 mg/L [5]. Excessive use of sodium chloride in food can cause several health problems such as vomiting, nausea, and headache.

It is a requirement by the EPA to monitor the concentration level of sodium at every entry point in the water distribution system [5]. The public health community needs to have information about sodium levels in drinking water that are supplied by various commercial water treatment facilities [4]. Some specific entry points of these water treatment plants require continuous measurements of the sodium chloride concentration level.

Sea water is one of the most common sources of salty water where the concentration level of sodium chloride is 35,000 ppm [9]. To maintain the ecological environment in water, it is required to maintain a certain concentration level of sodium chloride. It is very important to monitor the concentration level of NaCl in seawater for the oceanographers and marine biologists. One of the requirements of this research includes the lifetime of the sensor that measures the concentration. When the sensor is in direct contact with the sea water, its sensitivity degrades with time. In this project, the sensor is able to measure the concentration of NaCl without being in direct contact with the water. Thus, the sensitivity will not degrade with time and the lifetime of this sensor is expected to be very long.

Sodium is one of the richest elements in soil and needs to be monitored for agricultural purposes. In the United States, the concentration of sodium ranges from 500 parts per million (ppm) to 100,000 ppm. It is found in the soil and other surface materials [5]. Sodium is a major component for pesticides and is used frequently in the agricultural field for better production of crops. However, farmers need to know the concentration level of sodium to maintain the quality of the soil.

Sodium is one of the main elements of a water softener. A water softener is usually used to remove certain metal cations (calcium, magnesium) using the ion exchange process. Hard water can cause several problems such as pipes clogging with minerals built up inside of the pipe, scumming of soap, hair and skin damages. Using a water softener helps to get rid of these problems. But, as the water softening process follows the ion exchange principle, a certain amount of sodium ions exist in the water after the softening process [10] Using this water for a long period of time may cause

health problems. For these reasons, it is required to monitor the concentration of the sodium after the softening process. Embracing this fact, water softener companies are trying to include another section within the water softener device that will monitor the water quality after the softening process [11].

1.3 Motivation of research

The need for clean drinking water is ubiquitous and maintaining the safe drinking water standards established by the EPA is of the utmost importance for drinking water providers and consumers, both for health and legal reasons. Drinking water providers are required by law to frequently test their water supplies for contaminants at multiple stages of water treatment and transportation. There are a variety of methods companies can choose from to ensure that their drinking water meets the necessary standards.

There is a need for a water sensor that can detect changes in water quality in real time. The sensor should be able to detect the presence of contaminants instantly, without touching the water or without any mechanical movement. The sensor lifetime should be high, and it may require less maintenance over time and will not need to be replaced as often. These significant requirements are the motivation of this research project.

1.4 Different methods of water contaminant detection

Current technologies for water contaminant detection include Ion Chromatography (IC), Mass Spectrometry (MS), Fluorescence Spectroscopy, Atomic Absorption Spectroscopy, Inductive Coupled Plasma Mass Spectrometry (ICP-MS), and

Electrochemical Analysis (EA). Detection methods can vary depending on the measurement parameters. In this section, three different water contaminant detection methods are described.

1.4.1 Ion Chromatography

Ion chromatography is one of the most popular methods to detect proteins and inorganic charged compounds in drinking water. It is widely used in water treatment plants to detect various charged particles and their concentration. It is also used to separate different proteins.

Ion chromatography is a method of separation and quantitative analysis of anions and cations in a liquid solution [12]. Figure 2 shows the schematic diagram of the working principle of the ion chromatography method. This technique is based on the reversible adsorption of charged solute molecules to immobilized groups of opposite charge. The main condition of this method is the requirement of the sample solution to be polarized or charged [13]. The ion chromatography process includes four different stages: equilibration, sample application and wash, elution, regeneration.

Ion chromatography can be divided into two types: anion exchange and cation exchange chromatography. In anion exchange chromatography, the concentration of anion as a molecule of interest is determined whereas, in cation exchange chromatography, cation concentration is detected. The exchange of charged particles depends on the interaction of mobile phase and a secondary phase. The stationary phase (resin) is fixed, and the mobile phase (eluent) is moving. The stationary phase (resin) is added to the chromatography chamber to attract ions. The element of the stationary phase

depends on the anion or cation exchange chromatography. These two phases interact with each other and this interaction varies with different molecules. Based on this variation, which molecule will elute from the chamber faster than the other molecule differs.

In cation exchange chromatography, the negatively charged molecules are a stationary phase and used to attract the positive ions of the sampled solution. The chromatography process separates different ions inside of the liquid sample based on the difference in compound's partition coefficient. After the ions of interest leave the separation chamber, they are measured by an electrical conductivity detector. The result of the detector is a plot of conductivity vs. time. The individual ions generate separate peaks and the height of the peak depends on the relative ion concentration of the sampled solution. Using this method, the minimum detectable limit is a few parts per billion (ppb) [14]. Table 1-1 shows the minimum detection limit for various ions using the ion chromatography method from "Materials Evaluation and Engineering, INC" [14].

Table 1-1. Detection limit for Ion Chromatography method.

Cations	Minimum detection limit (ppb)	Anions	Minimum detection limit (ppb)
Lithium (Li^+)	1	Fluoride (F^-)	4
Sodium (Na^+)	5	Chloride (Cl^-)	20
Ammonium (NH_4^+)	5	Nitrite (NO_2^-)	20
Potassium (K^+)	8	Bromide (Br^-)	20
Magnesium (Mg_2^+)	7	Nitrate (NO_3^-)	20
Calcium (Ca_2^+)	7	Phosphate (PO_4^{2-})	20

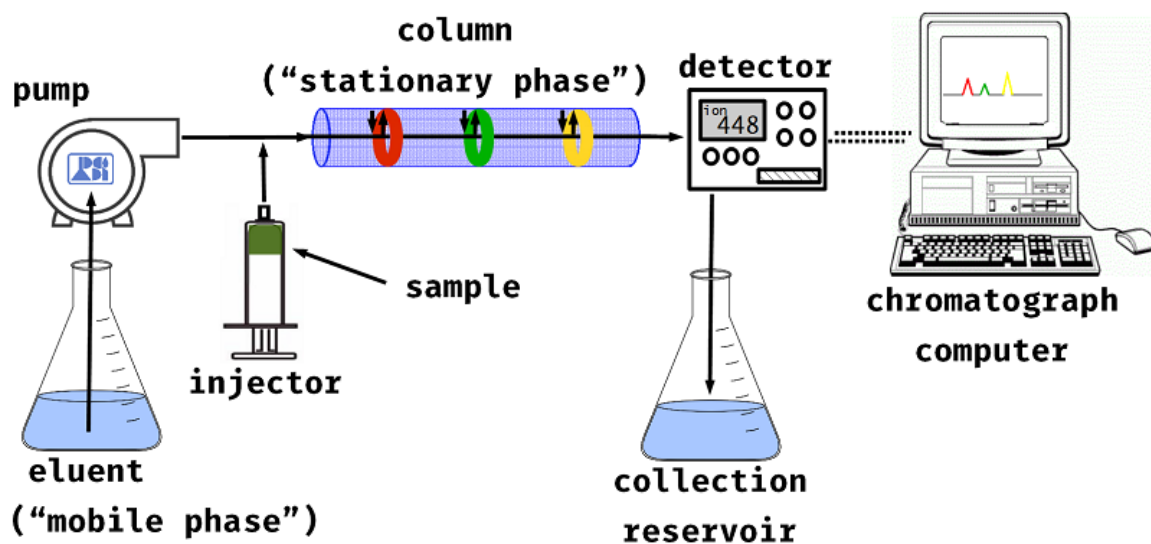


Figure 2. Working principle of Ion Chromatography method [15].

Although ion chromatography is very popular for water contaminant detection, there are several issues related to this method. This method is only valid for ionic components and proteins. The samples are required to be soluble in a solution. Most of the ion chromatography performance is attributed to the quality of the deionized (DI) water used to prepare eluents, standards, and samples. When the eluents flow out from the column and enter into the conductivity detector, it degrades the column efficiency of the chromatographer. Maintaining the pH level of the secondary phase is another challenge in this method.

1.4.2 Mass Spectrometry

Mass spectrometry is an analytic technique that identifies unknown chemical components from their complex (mixed with different chemical compounds) samples using their mass-to-charge ratio [16]. In this method, chemical components are converted

into ions and then the ions are sorted based on their mass. The uses of mass spectrometry include:

- Identifying various molecules in a mixture of sample solutions
- Identifying very small concentrations (Parts per billion, ppb) of metal contaminants in water samples
- Analyzing different protein contents, determining protein structures, functions, and interactions
- Determining the structures and functions of drugs and metabolites
- Measuring petroleum compositions
- Performing carbon dating

A mass spectrometer consists of three basic components. Figure 3 shows a schematic of the basic components of the mass spectrometer. The basic components are:

1. Ion source
2. Mass analyzer and
3. Ion detector

The following section includes the classification of mass spectrometers based on these three components.

The ionization sources can be classified by the following ways:

- Electron Ionization (EI)
- Chemical Ionization (CI)
- Atmospheric Pressure Chemical Ionization (APCI)
- Field Ionization (FI)
- Fast Atom Bombardment (FAB)

- Electrospray Ionization (ESI)
- Field Desorption Ionization (FDI)
- Plasma Desorption (PD)
- Matrix Assisted Laser Desorption Ionization (MALDI)
- Thermospray Ionization (TI)
- Atmospheric Pressure Ionization (API)

Mass analyzers can be classified by the following ways:

- Quadrupole Analyzers
- Ion Trap Analyzers
- Time-of-Flight Analyzers
- Magnetic and Electromagnetic Analyzers
- Ion Cyclotron Resonance and Fourier Transform Mass Analyzers

Ion detectors can be classified by the following ways:

- Photographic Plate
- Faraday Cup
- Electron Multipliers
- Electro-optical Ion Detectors

Based on the analysis of mixture, the mass spectrometer can be classified into:

- Gas Chromatograph (GC/MS)
- Liquid Chromatograph (LC/MS)

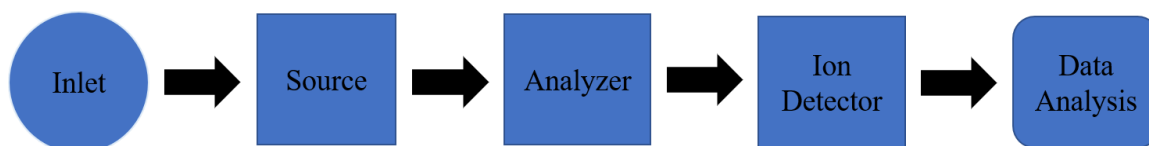


Figure 3. Schematic of the basic components of the Mass Spectrometer.

1.4.2.1 Basic Principle of operation of Mass Spectrometer

Figure 4 shows the working principle of a mass spectrometer. First, the sample is converted to the gas phase using heating methods. This vaporized sample then passes through the ionization chamber. In the ionization chamber, an electron beam is produced by a heated filament. This electron beam passes through the gas-phase sample to convert them into ions. By giving up electrons, these gas samples become ion state (positive ions). This process is called an electron impact (source). Most of the mass spectrometers work with positive ions. Electrons with energies around 70 eV are generally used for this bombardment process. With this energy, most of the ions will have a charge of +1. To produce a more positive charge requires more energy. During the whole procedure, the pressure is 10^{-5} to 10^{-8} Torr [17]. The vacuum state is an important condition as the ions are very reactive and should not react with any air molecules. Positively charged ions then go through the rest of the process when they face the ion repeller plate that is maintained at a slightly more positive charge. This section is called the acceleration state as the ions become a focused beam.

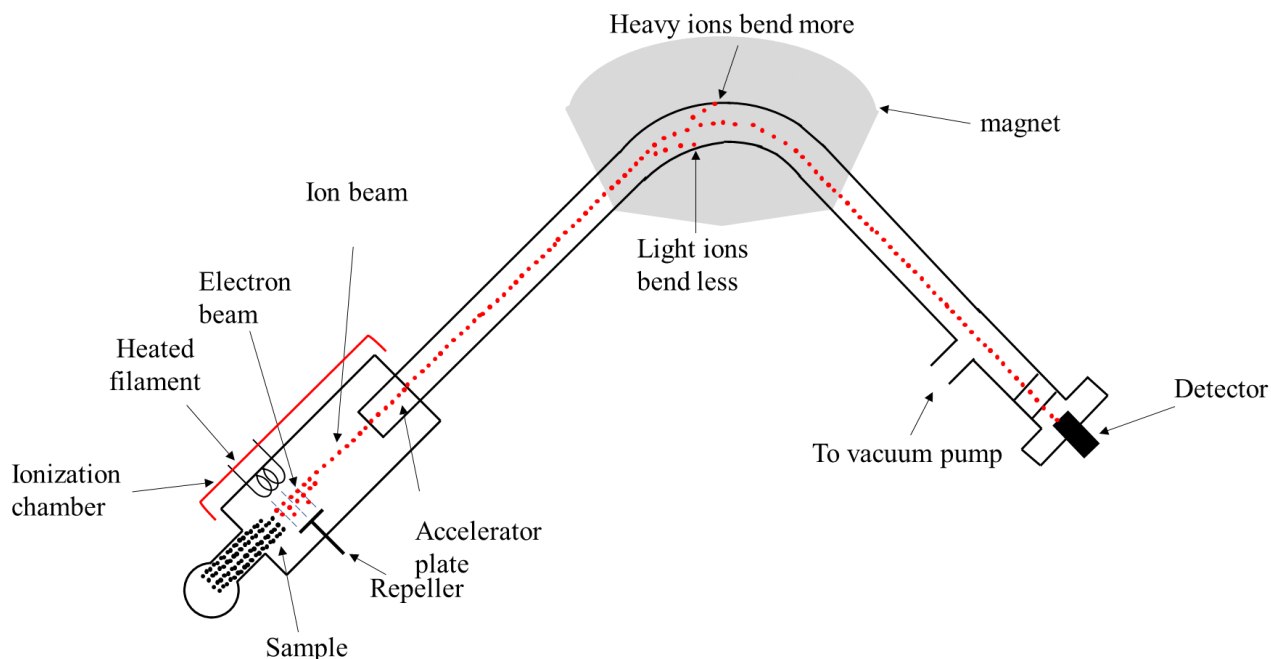
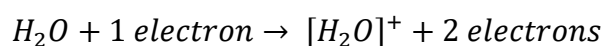


Figure 4. Working principle of a mass spectrometer [18].

When the positive ions pass through the magnetic field, they deflect. The deflection depends on the magnetic field, mass and charge of the ions. The deflection happens in an arc whose radius depends on the mass of each ion (mass-to-ion ratio). For example, ions with less mass will deflect more than the ions with heavy mass and ions with more charge will deflect more than ions with less charge.

The deflected ions are then focused to an ion detector. When the ions hit the metal wall of the detector, they become neutralized by receiving electrons from the metal. When the electrons inside of the metal try to reach equilibrium, they flow and are detected as a current. The more the positive ions hit the detector wall, the more current is generated. This process is called ion detection. Based on the component of interest and mass to charge ratio, one can change the magnetic field to change the deflection and collect the desired ions to the detector.

For example, if we take water (H_2O) as a sample, we can detect the number of its constituent components using a mass spectrometer. The water sample will be converted into water vapor and then a beam of electrons will pass through it. Because of this bombardment, a water molecule will produce a positively charged ion. With very high-powered bombardment it is possible to break the water molecule into fragments and produce $[H_2O]^+$, $[O]^+$ and $[H]^+$.



In the detector, the spectrum of different ions will show peaks with different heights and by analyzing the data, it is possible to find out the different components of the water sample and their relative concentration. Figure 5 shows the schematic result of the constituent component of a water molecule (H_2O) from the mass spectrometer.

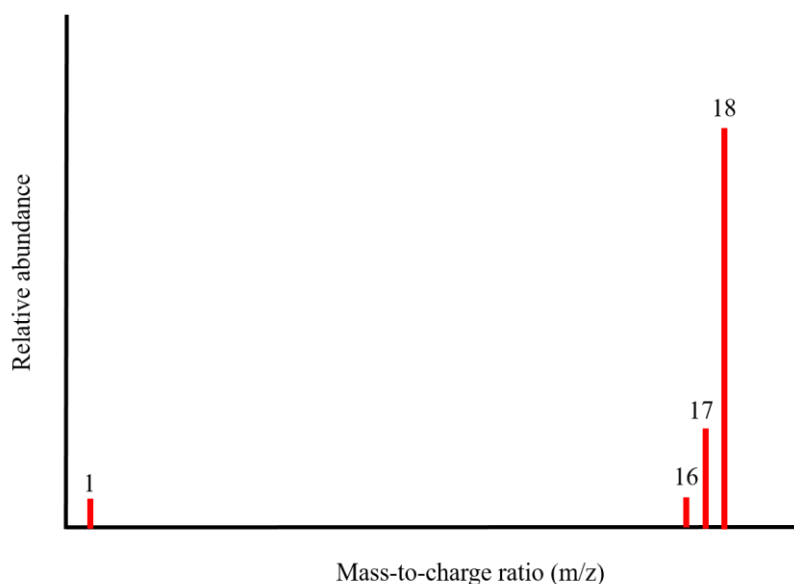


Figure 5. Spectrum analyzer analysis of a water sample.

Although mass spectrometry is a well-established technique, it has some limitations. Solution preparation is a challenge in this technique. The sensitivity of the measurements highly depends on detector performance. It is also difficult to identify the isomers of a compound having the same charge-to-mass ratio.

1.4.3 Atomic Absorption Spectroscopy

Atomic absorption spectroscopy (AAS) is an analytic method used to detect the concentration of an element (metal) from a mixed sample solution. This method is based on the absorption of optical radiation by the element of interest in the gaseous state. The selectivity of different elements depends on the absorption of different wavelength radiation. This technique is extensively used for monitoring, various contaminants and their detection limit inside of river water, seawater and drinking water. The usual detection limit using this technique is parts per billion (ppb) [19].

The working principle of atomic absorption spectrometry includes three sections: atomization, absorption, and detection. Figure 6 shows the basic working principle of atomic absorption spectroscopy method.

Atomization: For the atomization of the sample element, first the sample is dissolved into a suitable solvent. Then the solution flows to the atomizer and the sample is atomized into the flame.

Absorption: A hollow cathode lamp consists of a tungsten anode and a cylindrical hollow cathode. The cathode is made with the same element of interest. The anode and cathode stay inside of a sealed glass tube filled with neon or argon inert gas. When a voltage is applied to the cathode lamp, it absorbs energy and emits a photon as a

form of light. This emitted light is applied to the vaporized sample and some of the light will get absorbed by the sample atoms. Each element absorbs and emits its own unique wavelength, and this is the key point of an AAS. Ground state electrons move to the excited state when they absorb a certain amount of energy. But electrons are very unstable at the excited states and move back to the stable ground state by decaying the same amount of energy as light (photon) with the same wavelength. A monochromator is introduced after this section to select one specific wavelength (the wavelength to detect the sample element).

Detection: After the selection through the monochromator, this light is introduced to the detector. The detector serves two functions: first, it detects the sample of interest (qualitative analysis); second, it determines its concentration (quantitative analysis). A calibration graph with a best-fit curve that goes through the origin point is used to determine the concentration of the sample. Figure 7 shows the general calibration graph of atomic absorption spectroscopy.

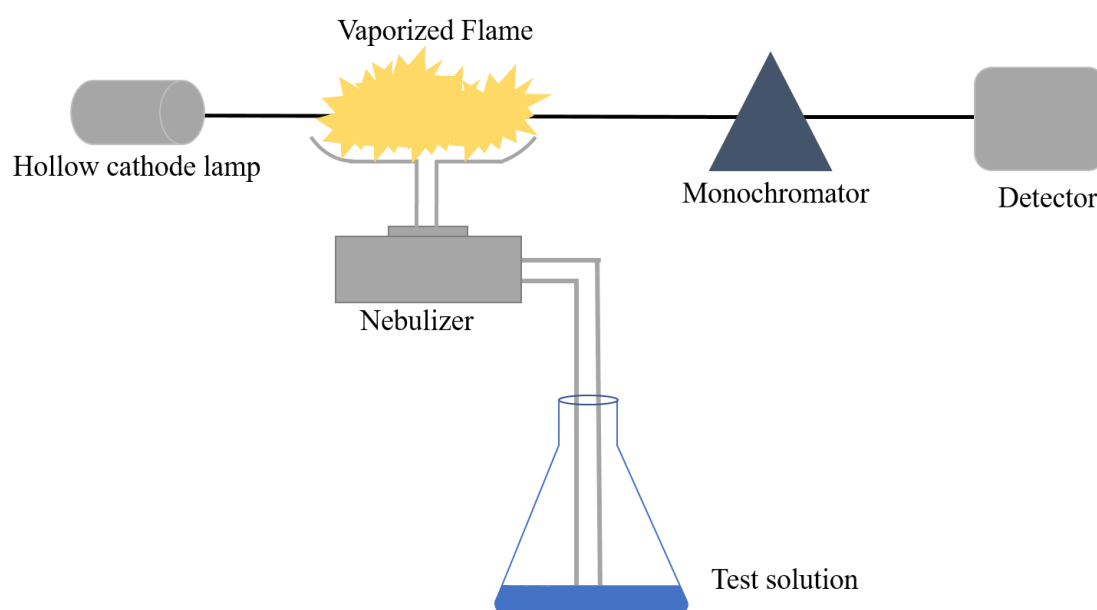


Figure 6. Working principle of Atomic Absorption Spectroscopy [20].

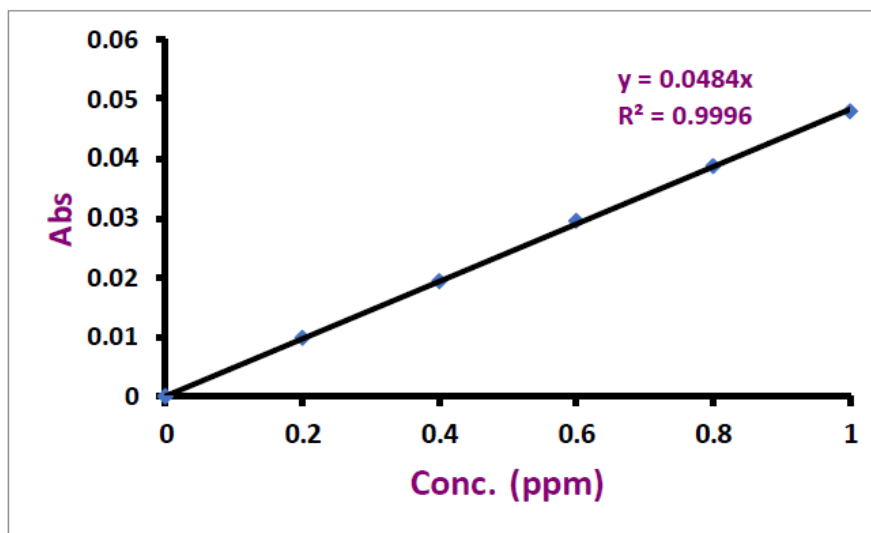


Figure 7. Typical calibration graph for Atomic Absorption Spectroscopy [21].

All three water contaminant detection technologies share some common limitations. The sample needs to be sent to the lab for the detection of contaminants. The techniques are not continuous and real-time measurements. Sample preparation is another critical issue for these techniques that require additional steps in which properties of the sample such as pH and actual concentration can change. All these methods require highly sophisticated machines and they are not portable. To overcome these bottleneck problems, new technology is required that can measure the water contaminants continuously in real-time with high sensitivity.

1.5 Approach

In this project, we are going to detect different salt solutions (NaCl, MgCl₂, the mixture of NaCl and MgCl₂) and their concentrations. The solutions are prepared using

solid salt samples mixed with DI water. A vector network analyzer (VNA) is used to measure the reflection coefficient (S_{11}) response.

Figure 8 shows a schematic design of the device. The device is built with a coil of magnetic wire that is mounted on the surface of a 1/4" pipe. The sample solution is placed inside of the pipe. Radio frequency signals are applied to the sensor using a vector network analyzer (VNA). Based on the contaminants inside of the sample solution, the signals are reflected. The VNA continuously calculates the reflection coefficient (S_{11}) from the ratio of the incident and reflected waves.

According to Ampere's law, the current flowing on a helical coil induces a magnetic field with the direction along the axis of the coil. A DC current creates a constant magnetic field whereas an AC current creates a time-changing magnetic field. As the magnetic field changes over time, an electric field is induced according to Faraday's law. The electric field causes ions to move in a circular fashion. The energy absorbed to create this motion alters the reflection coefficient (S_{11}) measurement.

The operating frequency in this measurement is 10MHz- 5GHz. Various contaminants have different resonant frequencies and the frequency shifts, amplitude, and phase changes are monitored to detect different contaminants and their concentrations. Contaminant selectivity and sensor sensitivity are improved by optimizing the sensor components. The measured reflection coefficient (S_{11}) data contains 20,000 amplitude and 20,000 phase values. The amplitude and phase information is used to train a machine learning algorithm. In this algorithm, a support vector regressor is trained with the S_{11} data and with that training, the algorithm calculates the concentration of the sample.

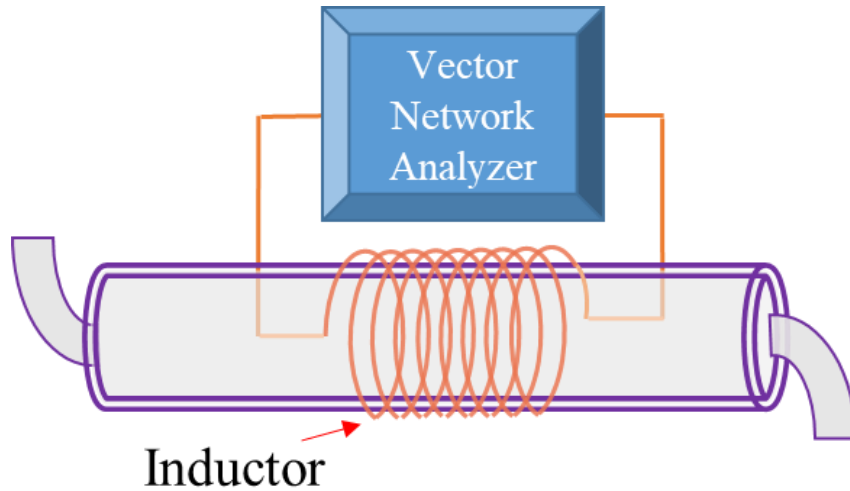


Figure 8. Schematic drawing of the experimental set-up.

1.6 Radio frequency signal

Microwaves are electromagnetic waves with a wavelength between 1 mm and 1m. The frequency response of different components depends on their physical dimension. The 1 GHz – 18 GHz frequency range is well established as the microwave frequency band. Table 1-2 shows the different frequency band designations with their corresponding frequency ranges [22]. In this project, the frequency range is considered from 10 MHz – 5 GHz. The corresponding wavelength ranges from 30 cm – 0.06 cm.

Table 1-2. Frequency band designations.

Frequency band designation	Frequency (GHz)
UHF	0.5 – 1
L	1 – 2
S	2 – 4
C	4 – 8
X	8 – 12
Ku	12 – 18

1.7 Thesis outline

This thesis is divided into six chapters. In chapter one, the thesis starts with introducing the importance of drinking water and monitoring different water contaminants to lead a healthy life. Different active methods for water contaminant detection are also described in this chapter. The next chapter deals with describing the basic elements of the sensor and the related working principles. In chapter three, the design parameters and measurement set-up are described with schematic diagrams and pictures. Chapter four includes the machine learning algorithm section where the operational procedure of the support vector regressor is explained. All the results and related discussions of the proposed technologies for water contaminant detection are included in chapter five. Chapter six contains the conclusion and future work of this project. A brief summary of each chapter is presented in the next few pages.

Chapter two starts with the basic understanding of the inductor and its equivalent circuit followed by the voltage-current relationship of an inductor. In that chapter, the quality factor (Q) for both series and parallel resonators is described. The effect of skin depth at the working frequency of this project is also explained for a better understanding of why the inductance of the sensor will change with different frequencies. A detailed explanation of the scattering matrix for a two-port network with emphasis on the reflection coefficient (S_{11}) is included in that chapter. At the end of that chapter, the Debye relaxation principle is described to explain the effect of an alternating field on the permeability and permittivity of the medium.

Chapter three begins with a fundamental description of the proposed device design parameters. Schematic diagrams and pictures of the sensor are provided for better

realization. The measurement set-up includes the sensor, inlet-outlet, faraday cage, and vector network analyzer. In that chapter, pictures are provided showing the whole device (inside of the faraday cage) connected to the network analyzer with SMA connector. After that, the solution preparation method is explained with equations and an example. The chapter ends with a brief description of the vector network analyzer.

Chapter four includes the basics of the machine learning algorithm. In this project, a support vector regressor is trained with k-fold validation method. A basic description of the support vector regressor is provided with related equations. The process employed to train the algorithm with measured reflection coefficient data is explained in that chapter. A flowchart explaining the steps of the algorithm is provided. At the end of that chapter, the optimization of the algorithm and error control methods are briefly discussed.

Results of this newly proposed water contamination method are presented in chapter five. This chapter is divided into three sections: the first and second sections contain the results with NaCl, MgCl₂ respectively, and the third section includes the result of NaCl and MgCl₂ mix solutions. The outputs of the machine learning algorithm are also included in all three sections. The basic principles to explain the mechanism of ion movement of our detection method is also discussed in this chapter.

This thesis also includes the conclusion and future work for this project. The implementation of this technology for heavy metal detection is explained as a part of the future work of this project. The feasibility of this technology for heavy metal (Pb) detection is also described.

CHAPTER 2 PRINCIPLE OF OPERATION OF INDUCTIVE SENSOR

This chapter is intended to provide a brief description of the basic principle of operation of an inductive sensor. The chapter starts by explaining the working principle of an inductor and its voltage-current relationship. Then, some important parameters such as Q-factor and skin depth are presented. After that, the formation of a scattering matrix is explained with emphasis on the forward reflection coefficient (S_{11}).

2.1 Inductive sensor

An inductive sensor is a device that is made of an inductor and uses the principle of electromagnetic induction. The non-contact behavior of the inductive sensor makes it particularly useful for applications where contact between the sensor and examined material presents challenges. Inductive sensors are usually not affected by media materials (oil, dust, and dirt) [23]. This characteristic makes them naturally suitable for harsh environments. Fast response, large operating temperature range, high reliability, robustness are the key advantages of inductive sensors [24]. In the next section, a detailed explanation of a typical inductor, its operating principle, and related characteristics are presented.

2.2 Inductor

An inductor is a passive two-terminal electromagnetic component. It consists of a wire wound into a coil around a core material. The core can be air or magnetic material

[25]. Figure 9 shows the circuit symbol for an air core inductor. The inductor resists changes in current by storing energy in the form of a magnetic field.

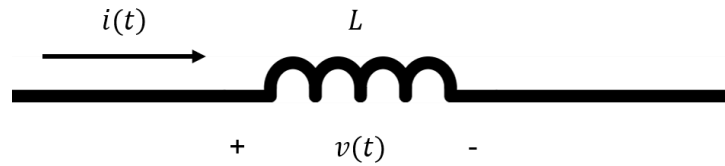


Figure 9. Circuit symbol of an inductor.

When alternating current flows through the inductor, according to Faraday's law, an induced electromotive force is created across the inductor [26]. According to Lenz's law, this induced voltage opposes the change in current that created it [27]. The ratio of the voltage change with respect to the rate of current change is described as inductance. Inductance is also known as the ability of an inductor to store energy. The unit of inductance is Henry (H). The typical range of inductance is $1\mu\text{H} - 0.1\text{H}$.

There are several types of inductors and they are used in various sectors of science and engineering. For example, RF coils are used in communication systems, switch mode inductors used in power supplies, differential, and common inductors in EMI filters [22]. Other primary applications of inductors include electric motors, transformers, sensors, and magnetic energy storage devices. Figure 10 shows an inductor mounted on the surface of a glass tube. One important fact about our sensor's sensing ability is the core material. In this project, liquid solutions are used along with a glass tube as a core material. The permeability of the combined core controls the inductance and the resonance behavior of the inductor.

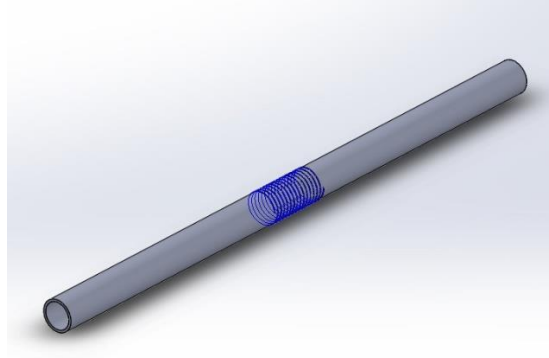


Figure 10. An inductor mounted on a glass tube.

2.3 The voltage-current relationship of an inductor

Let us assume a wire forms a loop as shown in Figure 11. The length of the wire is l . If a current $i(t)$ flows through the wire, it will generate a magnetic field, B . If μ is the magnetic permeability of the core material, then the magnetic field can be expressed as:

$$B(t) = \mu \frac{i(t)}{l} \quad (1)$$

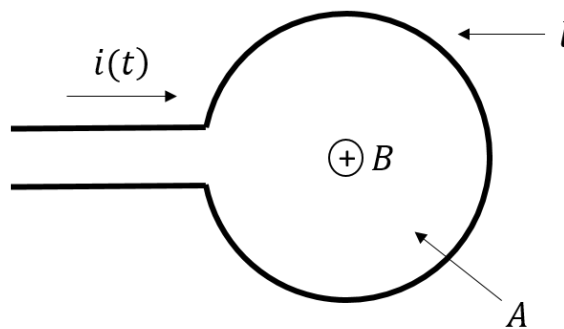


Figure 11. Cross-sectional view of the inductor with one turn.

Now, if we consider that the magnetic field, B is passing through a surface area of A , we can calculate the magnetic flux Φ_z in the z -direction using the following equation [28]

$$\begin{aligned}\Phi_z &= AB(t) \\ &= \frac{A\mu}{l} i(t)\end{aligned}\tag{2}$$

If the coil has N turns, then the magnetic flux becomes,

$$\begin{aligned}\Phi_z &= \frac{NA\mu}{l} i(t) \\ \Phi_z &= L i(t)\end{aligned}\tag{3}$$

Where L is the inductance and expressed as

$$L = \frac{NA\mu}{l}\tag{4}$$

From Maxwell's equation, we know that the terminal voltage $v(t)$ across the inductor is equal to the time derivative of the flux linkage. Thus,

$$\begin{aligned}v(t) &= \frac{d\Phi_z}{dt} \\ v(t) &= L \frac{di(t)}{dt}\end{aligned}\tag{5}$$

The amount of energy stored as a magnetic field in or around the inductor is governed by:

$$U = \frac{1}{2} Li(t)^2\tag{6}$$

2.4 Equivalent circuit model of an inductor

In this model, the coil is made of copper wire wound around the core material. This copper wire adds parasitic resistance (R) that is in series combination with the ideal inductance (L). The wire leads on both ends of the coil will introduce a parasitic capacitance (C) and they are in parallel combination with the ideal inductance (L) and parasitic resistance (R) [29]. The equivalent circuit model for an inductor is presented in Figure 12.

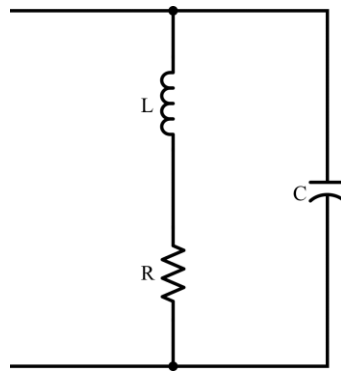


Figure 12. Equivalent circuit model of an inductor.

2.5 Q factor

The quality factor (Q factor) is an important parameter for inductive sensors. It relates the amount of energy loss relative to the energy stored for a resonant system. The energy is stored by the inductor and capacitor, and the energy is dissipated by the resistor of the system. High Q value implies a low loss in the system. The higher the Q factor, the closer its behavior as an ideal inductor. The Q factor can be expressed by the following equation [30]:

$$Q = \omega_r \frac{(\text{average energy stored})}{(\text{energy loss per cycle})} \quad (7)$$

Here, ω_r is the resonant frequency.

$$\omega_r = 2\pi f_r \quad (8)$$

Q factor is a measurement of loss and can be categorized into three types, depending on the characteristics of loss [30].

$$\text{Unloaded } Q: Q_U \equiv \omega_r \frac{\text{Energy stored in the resonant circuit}}{\text{Power loss in the resonant circuit}} \quad (9)$$

$$\text{Loaded } Q: Q_L \equiv \omega_r \frac{\text{Energy stored in the resonant circuit}}{\text{Total power loss}} \quad (10)$$

$$\text{External } Q: Q_E \equiv \omega_r \frac{\text{Energy stored in the resonant circuit}}{\text{Power loss in the external circuit}} \quad (11)$$

In the unloaded Q factor, no load is considered, and all the power loss is related to only the resonant circuit itself. The amount of coupling of the resonant circuit to the external circuitry is defined by the external Q. With the following equation, these three Q factors are related to each other [30].

$$\frac{1}{Q_L} = \frac{1}{Q_E} + \frac{1}{Q_U} \quad (12)$$

Figure 13 presents a series and a parallel LC resonant circuit. R and G are associated with the losses in the resonant circuits themselves. The Q factor for a series circuit is governed by the following equation [30].

$$Q_U = \frac{\omega_r L}{R} \quad (13)$$

$$Q_E = \frac{\omega_r L}{R_G} \quad (14)$$

$$Q_L = \frac{\omega_r L}{R + R_G} \quad (15)$$

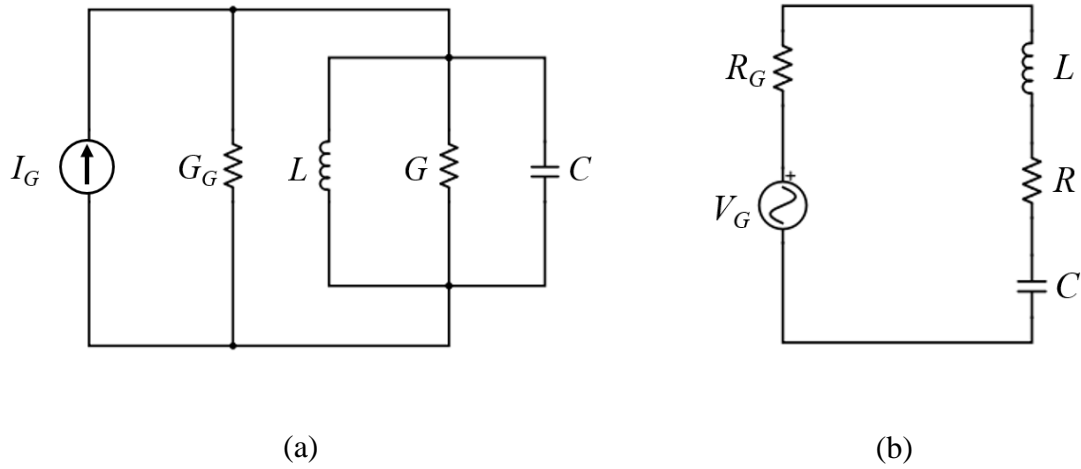


Figure 13. (a) Series and (b) parallel LC resonant circuit.

And for the parallel circuit [30]:

$$Q_U = \frac{\omega_r C}{R} \quad (16)$$

$$Q_E = \frac{\omega_r C}{G_G} \quad (17)$$

$$Q_L = \frac{\omega_r C}{G + G_G} \quad (18)$$

Q can also be calculated as the resonance curve full bandwidth Δf signal (full width at half maximum power) relative to its maximum frequency f_r [31]

$$Q = \frac{\Delta f}{f_r} \quad (19)$$

Using equation 19, calculated Q value of the device at 559.1 is 192.79 MHz when the device is filled with air (Figure 38).

2.6 Skin effect

When an AC signal is applied to an inductor, an alternating magnetic field is generated due to the alternating motion of charge carriers. According to Faraday's law, this alternating magnetic field will generate an induced electric field. The current density associated with this electric field will oppose the initial current flow and this effect is strongest at the center of the conductor. At high frequency, the electrons tend to travel through the outer areas of the conductor [32]. As a result, the current density becomes higher at the surface and tends to lower towards the center of the conductor. Reduction in the effective area for the current flow causes an increase in the resistance. This increment of resistance is a function of frequency, permeability, and conductivity. This phenomenon is known as the skin effect. Skin effect is more dominant at higher frequencies rather than lower frequency. In a conductor, the depth at which significant current flows is known as skin depth. The skin depth (δ) can be expressed as:

$$\delta = \sqrt{\frac{\rho}{\pi f \mu_r \mu_0}} \quad (20)$$

Where ρ is the resistivity of the material, f is the frequency, μ_r is the relative permeability and μ_0 is permeability constant ($4\pi \times 10^{-7}$). Using equation 20, at 5 GHz frequency, the calculated value of skin depth is 0.922 μm .

2.7 The Scattering Matrix

When the circuit dimensions are small compared to the wavelength, the voltage and current are unique at any point in the circuit and easy to measure. But, it is difficult to

measure the voltage and current for circuits operating at microwave frequencies. At microwave frequencies, the wavelength of the signals is comparable to the line length. Hence the line current and voltage are of different values at different points along the line [33]. Hence, at high frequency, equivalent voltage and current, related impedance and admittance matrices become difficult to determine. Scattering parameters (S-parameters) are commonly used to describe the performance of the device at microwave frequencies.

A scattering matrix is defined as the relationship between the voltage waves incident on the ports to those reflected from the ports. Figure 14 shows a simple transmission system with the incident, reflected and transmitted wave. Using the incident, reflected and transmitted waves, a scattering matrix is formed as a representation of the direct measurement of voltage and current.

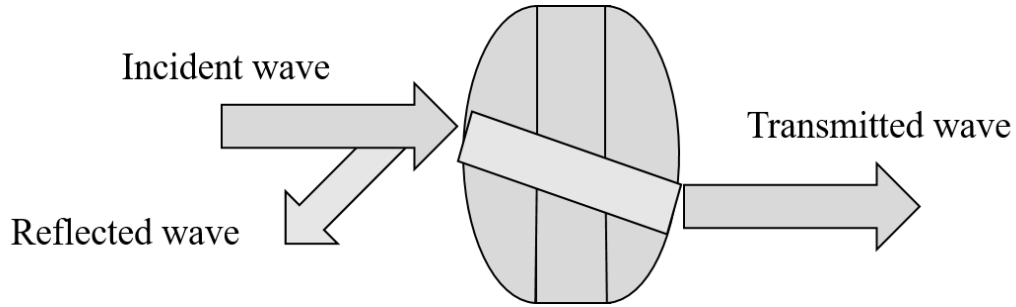


Figure 14. Simple transmission system [34].

An N-port device has N^2 S-parameters. Figure 15 shows the schematic representation of a two-port network. For a 2-port network, the matrix has the following formation [33]:

$$\begin{bmatrix} V_1^- \\ V_2^- \end{bmatrix} = \begin{bmatrix} S_{11} & S_{12} \\ S_{21} & S_{22} \end{bmatrix} \begin{bmatrix} V_1^+ \\ V_2^+ \end{bmatrix} \quad (21)$$

Here $[S]$ is called the Scattering matrix. A two-port network has four S-parameters. For S-parameters, the numbering convention is such that the signal that is

coming out of a port is the first number following the “S” and the signal that is applied to a port is the second number following the “S” [35]. So, S_{21} describes the relationship of voltage that is coming out from port two and applied to port one. When both numbers are the same it implies that the input and output ports are the same.

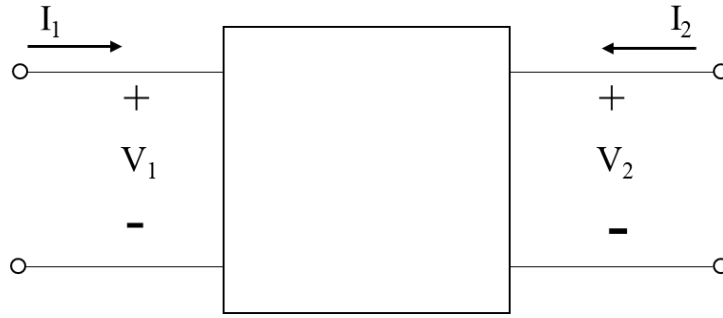


Figure 15. Two-port network.

S- parameters can be classified into two groups: reflection and transmission characteristics. The reflection characteristics of S-parameters are S_{11} and S_{22} and the transmission characteristics are S_{21} and S_{12} . In this project, the measurement parameter is S_{11} . All the S-parameters for a 2-port network can be defined as [34]:

$$\text{Forward reflection coefficient, } S_{11} = \frac{\text{reflected}}{\text{incident}} = \frac{V_1^-}{V_1^+} \Big|_{V_2^+=0} \quad (22)$$

$$\text{Reverse reflection coefficient, } S_{22} = \frac{\text{reflected}}{\text{incident}} = \frac{V_2^-}{V_2^+} \Big|_{V_1^+=0} \quad (23)$$

$$\text{Reverse transmission coefficient, } S_{12} = \frac{\text{transmitted}}{\text{incident}} = \frac{V_1^-}{V_2^+} \Big|_{V_1^+=0} \quad (24)$$

2.8 Forward Reflection coefficient (S_{11})

S_{11} is called reflection coefficient and is defined as the ratio of the amplitude of the reflected voltage at port one with respect to the input voltage at port one. It is a figure that quantifies the impedance discontinuity in a transmission medium. The Greek letter, Γ is used to symbolize the reflection coefficient. It is a complex quantity and the magnitude portion of Γ is called ρ (rho) and the phase portion is denoted with ϕ [33].

$$\text{Reflection coefficient, } S_{11} = \Gamma = \frac{V_{reflected}}{V_{incident}} = \rho \angle \phi = \frac{Z_L - Z_0}{Z_L + Z_0} \quad (25)$$

$$\rho = |\Gamma| \quad (26)$$

Here, Z_L is the load impedance and Z_0 is the transmission line impedance. When line impedance is equal to the load impedance, then all the energy will be transferred to the load and nothing will be reflected back resulting $V_{reflected} = 0$ and $\Gamma = 0$. When Z_L is an open or short circuit, then all the energy is reflected back and $\Gamma = 1$. When Z_L is not equal to Z_0 , then some of the incident wave will be reflected back and the magnitude of the reflection coefficient will be in the range between 0 and 1. In this project, the reflection coefficient (Γ) is measured in a log-magnitude and expressed in terms of dB. Another way to express the reflection coefficient as return loss and governed by the following equation [34]:

$$\text{Return loss} = -20 \log(\rho) [dB] \quad (27)$$

The negative sign in the equation 27 implies that the return loss is always a positive value. The return loss value ranges from infinity for Z_0 impedance and 0 dB for short or open circuit [34].

In this project, we are measuring the reflection coefficient of the device filled with air, DI water, and salt solutions (NaCl, MgCl₂, and mix of NaCl and MgCl₂). These materials are considered as a complex dielectric medium for the inductive sensor. When an external oscillating electric field is applied to the dielectric medium, a momentary delay is found in the dielectric constant of the material, due to the molecular polarization [36]. This phenomenon is called dielectric relaxation and can be explained with the Debye relaxation theory, Cole-Cole model, Cole-Davidson model, and Havriliak-Negami model. In the next section, brief descriptions of all these models are presented.

2.9 Dielectric relaxation

Polarization is one important phenomenon for dielectric materials. When a dielectric material is subjected to an alternating electric field, a change in the distribution among its molecular and atomic charges takes place [36]. This distribution produces a very small current. This small current is defined as a dielectric loss. The particles, ions or molecules of that material face small movements and displacements and lose their equilibrium. When the applied electric field is removed, the constituents of the dielectric medium will try to reestablish the equilibrium. The change in the equilibrium state is not an instantaneous process [36]. There exists a delay in molecular polarization and the time required for the material to respond to the applied electric field is called dielectric relaxation time. The polarization of each dielectric material depends on the nature of its molecular and atomic chemical bonds [36].

To explain the dielectric mode, Debye proposed a model in 1929 that explained the dielectric relaxation for some materials [37]. In this model, Debye considered a

unique relaxation time for all molecules. According to the model, the complex dielectric constant is given by [36]:

$$\tilde{\varepsilon} = \varepsilon' - i\varepsilon'' \quad (28)$$

Where ε' and ε'' are called dielectric constants (or loss factors). The final Debye relaxation formula has the following expression [36]:

$$\tilde{\varepsilon}(s)_D = \frac{\varepsilon^*(s) - \varepsilon_\infty}{\varepsilon_0 - \varepsilon_\infty} = \frac{1}{1 + s\sigma} \quad (29)$$

Where $\tilde{\varepsilon}(s)_D$ is the complex susceptibility, ε^* is the complex permittivity of the dielectric, the real value ε_0 is the low frequency dielectric constant, the real value ε_∞ is the high frequency dielectric constant and σ is the constant associated to the dipole's characteristic relaxation time.

The Cole-Cole model updated Debye's model based on experimental data on dielectric materials. That model shows more appropriate results when the dielectric loss peaks show symmetric broadening. The Cole-Cole equation is given by [36]:

$$\tilde{\varepsilon}(s)_{CC} = \frac{1}{1 + (s\sigma)^\alpha} \quad (30)$$

Where α is a parameter which can have values between 0 and 1.

Cole-Davidson collaboration proposed an almost complete determination model for dielectric properties of the materials. Their model was based on the experiments on dielectric liquids glycerol and propylene glycol. They proposed the following equation [36]:

$$\tilde{\varepsilon}(s)_{CD} = \frac{1}{(1 + s\sigma)^\beta} \quad (31)$$

Where $0 < \beta \leq 1$.

Havriliak-Negami model proposed a more detailed expression to describe the dielectric relaxation which generalizes the dispersion models of Debye, Cole-Cole, Cole-Davidson. The expression is [36]:

$$\tilde{\epsilon}(s)_{HN} = \frac{1}{(1 + (s\sigma)^\alpha)^\beta} \quad (32)$$

From the equation 32, it can be observed that, when $\beta = 1$, we can obtain the Cole-Cole mode, when $\alpha = 1$, we have the Cole-Davidson model and for $\alpha = \beta = 1$, we obtain the Debye relaxation model.

2.10 Ion responses of an AC coil

In this section, a detailed explanation is presented to understand the reflection coefficient response for different salt solutions (NaCl, MgCl₂, NaCl + MgCl₂). Faraday's law, Ampere's law, and Lorentz force law are applied to explain these phenomena.

\vec{H} Near coil Center:

Let us consider that the glass tube acts as a cylinder as shown in Figure 16 and the inductor is mounted on the surface of the cylinder. When a signal is applied to the coil, within the cylinder, the magnetic field strength, \vec{H} is uniform across the area. \vec{H} exists only in the z direction (except near the ends of the cylinder).

According to Ampere's law to find \vec{H} in the cylinder:

$$\oint \vec{H} \cdot d\vec{l} = I_{enc} \quad (33)$$

$$\vec{H} = H_z \hat{e}_z \quad (34)$$

In equation 33, I_{enc} represents the current distribution in the enclosed loop. Figure 16 shows a cross-section of the tube, current distribution across the tube and all the considered directions. We can consider that the loop is a rectangle. Now, H_z can be presented as:

$$H_z = \frac{N}{d} I \quad (35)$$

We can also describe H_z as the current times the number of turns per meter.

H_z depends on the ratio of length to diameter (l/D) of the coil. If l/D is large, then H_z is flat over the cylinder length and drops quickly outside the cylinder. And, if l/D is small, then H_z is not uniform but is strongest in the center and decreases towards the ends. In this project, the coil can be considered to have large l/D .

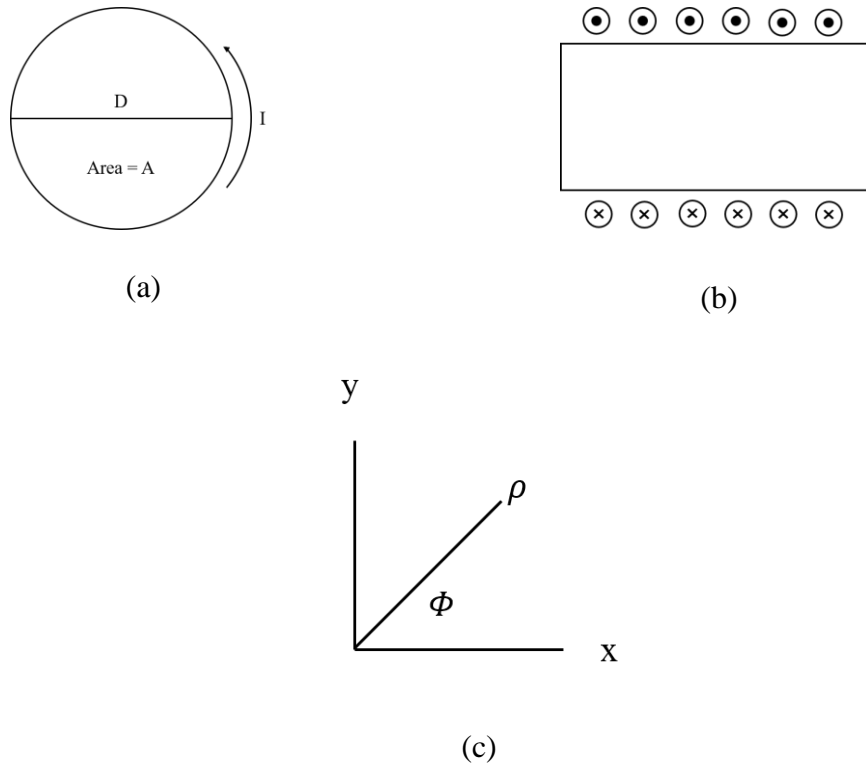


Figure 16. (a) Cross section of the tube (b) charge distribution across the tube (c) coordinate system.

Coil with AC current:

If the coil dimensions are small compared to the wavelength, then \vec{H} remains the same as the DC coil case. However, since \vec{H} and hence \vec{B} are changing with time, an electric field is induced.

The electric field \vec{E} can be found using Faraday's law:

$$\text{Differential form: } \nabla \times \vec{E} = -\frac{\partial \vec{B}}{\partial t} \quad (36)$$

$$\text{Integral form: } \oint_l \vec{E} \cdot d\vec{l} = -\frac{\partial}{\partial t} \int_s \vec{B} \cdot d\vec{S} \quad (37)$$

Since \vec{B} is in the z direction, we choose a loop in the x - y plane with radius ρ .

Then, the surface has direction \hat{e}_z . The electric field \vec{E} is expected to be in the Φ direction and depend on ρ .

$$\vec{E} = E_\Phi(\rho) \hat{e}_\Phi \quad (38)$$

Let $\vec{B} = B_z \cos \omega t \hat{e}_z$. Then, using Faraday's law (differential form), we have,

$$\nabla \times E_\Phi(\rho) \hat{e}_\Phi = -\frac{\partial B_z \cos \omega t \hat{e}_z}{\partial t} \quad (39)$$

$$E_\Phi 2\pi\rho = -\frac{\partial [(\pi\rho^2)B_z \cos \omega t]}{\partial t} \quad (40)$$

Solving for E_Φ :

$$E_\Phi = \frac{\omega B_z}{2} \rho \sin \omega t \quad (41)$$

From equation 41, it can be noticed that:

- E_Φ increases as ρ increases
- E_Φ is 90° out of phase from \vec{B}
- It can be shown that the units are correct:

$$\omega B_z \rho : [V/m] \quad (42)$$

Charged Ion in DC Current Coil:

When a magnetic field is applied to a charge, the force exerted on it is found by:

$$\vec{F} = q(\vec{v} \times \vec{B}) \quad (43)$$

If the charged ion is traveling in the z -direction (the expected case), then the force is zero.

If the ion has a component of \vec{v} in the ρ direction, the particle circulates in the $-\hat{e}_\phi$ direction, travelling in a helix as it flows through the tube. As v_ϕ increases, the interaction with \vec{B} causes the radius of the helix to get smaller.

Charged Ion in AC Current Coil:

In the AC case, charged ions experience a force due to \vec{E} , which is in the $+\Phi$ direction. The force creates ion motion in the Φ direction.

$$\vec{F} = q\vec{E} = qE_\phi \hat{e}_\phi \quad (44)$$

If we assume only one ion with charge Q at a particular ρ location, then,

$$\vec{F} = Q \frac{\omega B_z}{2} \rho \sin \omega t \hat{e}_\phi \quad (45)$$

A negative charge would have moved in the $-\hat{e}_\phi$ direction and the force on the negative ion would be in the opposite direction as a positive ion.

Effect on S_{11} :

The interaction between the electric field induced by the AC coil and a charged ion results in a force on the ion. Force requires energy. Therefore, the energy absorbed to create the force is not reflected back to port 1 of the VNA.

Forces in the ion cause charge in motion, which is current. Current density is defined as:

$$\vec{J} = \rho_v \vec{v} \quad (46)$$

$$I\hat{e}_v = Q\vec{v} \quad (47)$$

Velocity can be obtained from the mobility. Mobility is the conversion between electric field and velocity. Force due to \vec{E} results in acceleration which causes particles to move and quickly reach a terminal velocity. In conductors, there is the electron mobility (μ_e). In liquids, we use the ionic mobility μ_i .

Therefore, \vec{E} in the Φ direction causes a current to flow:

$$I\hat{e}_v = Q\vec{v} = Q\mu_i E_\phi \hat{e}_\phi \quad (48)$$

Interaction of $I\hat{e}_v$ with \vec{B} :

The force produced by $I\hat{e}_v \times \vec{B}$ is:

$$\vec{F} = Q\mu_i E_\phi \hat{e}_\phi \times B_z \cos \omega t \hat{e}_z \quad (49)$$

Substituting for E_ϕ , we find:

$$\vec{F} = \frac{1}{2} Q\omega B_z^2 \mu_i \rho \sin \omega t \cos \omega t \hat{e}_\rho \quad (50)$$

Using a trigonometric identity, the final result is:

$$\vec{F} = \frac{1}{4} Q\omega B_z^2 \mu_i \rho \sin(2\omega t) \hat{e}_\rho \quad (51)$$

Equation 51 indicates that:

- Positive and negative ions produce current in the same direction, so the force is the same for both.
- The force depends on B_z^2 and ρ
- The force is in the ρ direction, causing fluctuations in the location in ρ over time along with the Φ fluctuations due to the interaction of the ion with \vec{E} .

The total force (primary and secondary effects) is:

$$\vec{F} = \frac{1}{4} Q \omega B_z [2\rho \sin \omega t \hat{e}_\phi + B_z \mu_i \rho \sin \omega t \hat{e}_\rho] \quad (52)$$

The total force has two components: a Φ component and a ρ component. Force to move the ion requires energy. Absorbed energy results in less return signal and therefore a drop in S_{11} .

CHAPTER 3 DEVICE DESIGN AND MEASUREMENT SET-UP

3.1 Device parameters

In this section, the device parameters of the sensor (inductor) and tubing system with inlet and outlet information are given. Figure 17 shows the top, side, and cross-sectional views of the sensor. We made a holder with an acrylic plate to hold the device. Figure 18 shows a side view of the sensor on the holder.

Inductor:

Wire length: 32 cm

Wire diameter: 0.035 cm

Coil length: 1.15 cm

Coil diameter: 0.67 cm

Solenoid length to diameter ratio: $1.15/0.67=1.71$

Winding pitch: $1.15/16=0.07\text{cm}$

No. of turns: 16

Space between two turns: 0.035cm

Wound in a single layer

Wire material: Copper; Insulation: Insulation base coat (modified polyester resin)

Inductance of coil- 0.768 μH

Glass tube:

Outer diameter: 0.635 cm

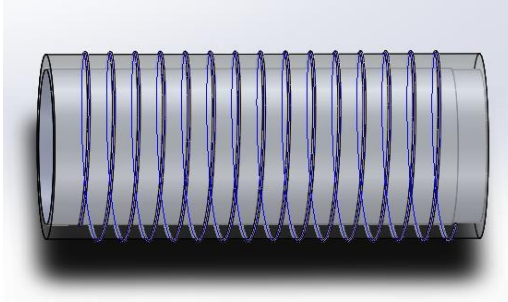
Inner diameter: 0.535 cm

Inlet and Outlet tube:

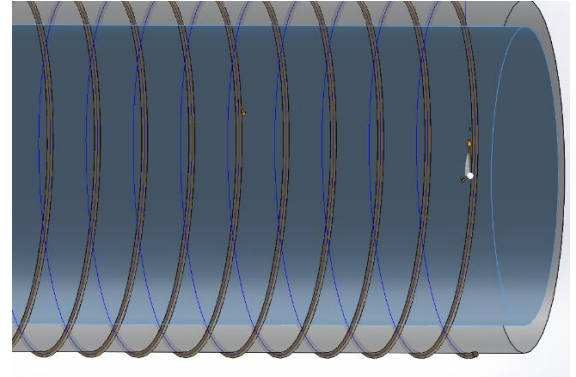
Tube type: PVC tubing

Outer diameter: 0.635 cm

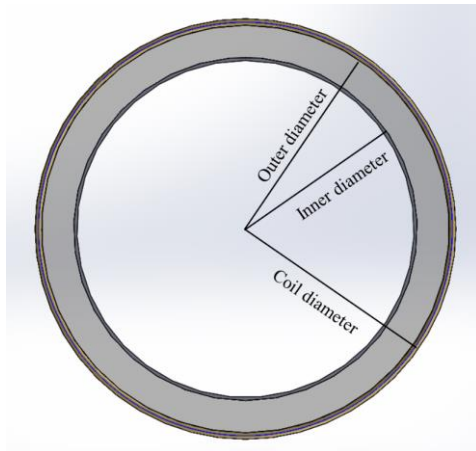
Inner diameter: 0.535 cm



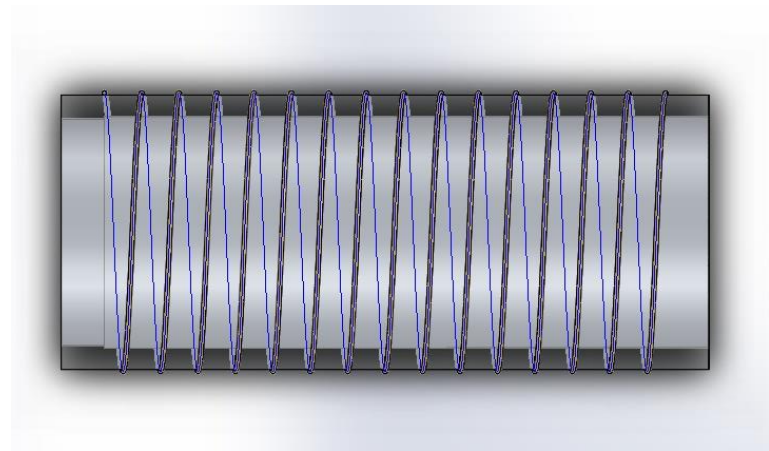
(a)



(b)



(c)



(d)

Figure 17. (a) Side view of the sensor (b) Coil structure (c) Cross-sectional view of the sensor (d) Top view of the sensor.

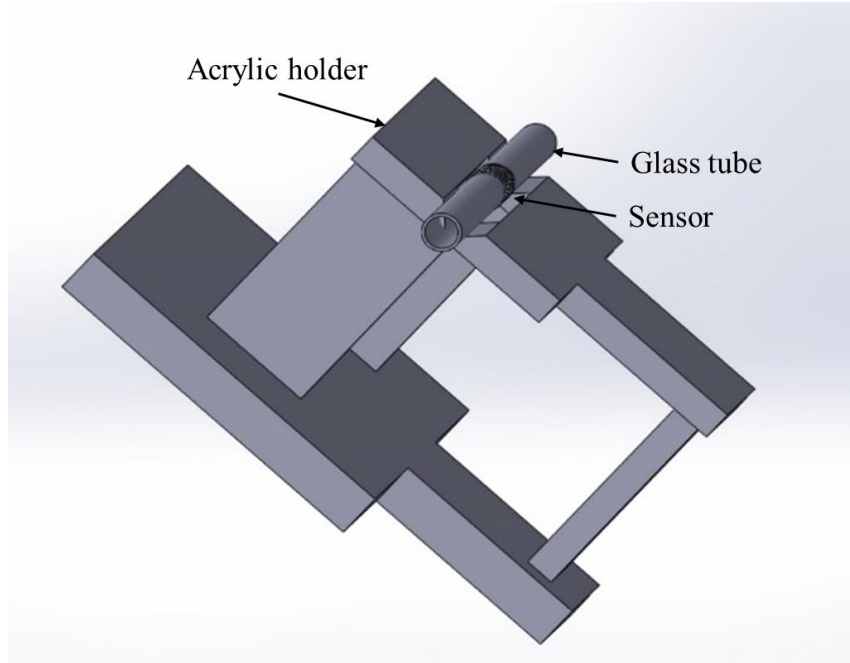


Figure 18. Device structure.

3.2 Inductance calculation

Inductance is described as a property of an electrical conductor to oppose a change in the electric current that flows through it [38]. There are three models that one can use to calculate the inductance. They are the Rosa-Nagaoka method of the American National Bureau of Standards (NBS), the Kirchhoff summation method found from Maxwell's mutual inductance formula, and the Chester Snow model [39]. Among these three models, the Chester Snow model considers the helicity property of an inductor to calculate the inductance. David W Knight presents a detailed calculation of solenoid inductance considering several solenoid parameters that are usually neglected. The final equation for solenoid inductance is [39]:

$$L = \mu \frac{\pi r^2}{l} N^2 K_H \quad (53)$$

$$\text{where, } K_H = K_L - \frac{2}{\pi} (l/D) \frac{\left(K_M + K_{S(x)} - \frac{(\mu_i/\mu_x)\Theta}{4 \cos \psi} \right)}{N} \quad (54)$$

Where,

L = solenoid inductance

N = number of turns in coil

l = solenoid length

r = effective loop diameter (or radius)

K_L = field non – uniformity correctrion for short coil

K_m = mutual inductance correction for round wire

$K_{S(x)}$ = self inductance correction for round wire

μ_i = permeability of the wire material

μ_x = permeability of the medium outside the conductor

Θ = inductance factor

3.3 Self-resonance frequency calculation

The principal self-resonance frequency (SRF) of an air-cored solenoid occurs when the wire length is approximately $\frac{\lambda}{2}$ [40]. Equation 55 shows the formula to calculate the principal self-resonance frequency. Using this equation, the first resonance frequency of our sensor is found to be around 446 MHz.

$$\text{Principal SRF: } f = \frac{v}{\lambda} = \frac{v}{2l_w} \quad (55)$$

No. of turns in coil: 16

Coil diameter: 0.0067m

Length of the conductor of the coil, l_w : $16 \times 3.1416 \times 0.0067 = 0.336$ m

Now,

$$\frac{\lambda}{2} = 0.336$$

$$\lambda = 0.672 \text{ m}$$

$$\frac{v}{\lambda} = f \quad (56)$$

$$f = \frac{3.0 \times 10^8}{0.672} = 446 \text{ MHz}$$

First self resonance frequency of the sensor = 446 MHz

However, because of the parasitic capacitance, the first resonance frequency of the sensor is found experimentally at 413.9 MHz. To calculate the self-capacitance of the sensor, we can follow the formula presented by David W Knight [40],

$$\frac{C_L}{D} = \frac{4\epsilon_0\epsilon_x}{\pi} \left(l/D \right) \left[1 + \frac{\left(1 + \frac{\epsilon_l}{\epsilon_x} \right)}{2} \left(\frac{1}{K_L} - 1 + \frac{\pi(l/D)}{\ln(1 + \pi^2 l/D)} \right) \right] \frac{1}{\cos^2 \psi} \quad (57)$$

Where,

C_L = self – capacitance

l = solenoid length

D = average diameter (inside coil diameter + wire diameter)

l/D = length to diameter ratio

ε_i = relative permittivity on the inside

ε_x = relative permittivity external to the solenoid

K_L = long current – sheet approximation

ψ = pitch angle

3.4 Measurement set-up

In this project, the sensor is soldered to a pair of copper strip lines. Copper strips are used to improve the stability of the sensor. Then, the copper strip lines are soldered to an SMA connector. The SMA connector connects the sensor to the vector network analyzer. Figure 19 shows the top pictorial view of the sensor. The inductor is mounted on the outer surface of a $(1/4)$ " inch glass tube. Both ends of the glass tube are connected with “quick-connect” to attach the inlet and outlet tubing system. The inlet and outlet tubing are polyvinyl chloride (PVC) based tubes.

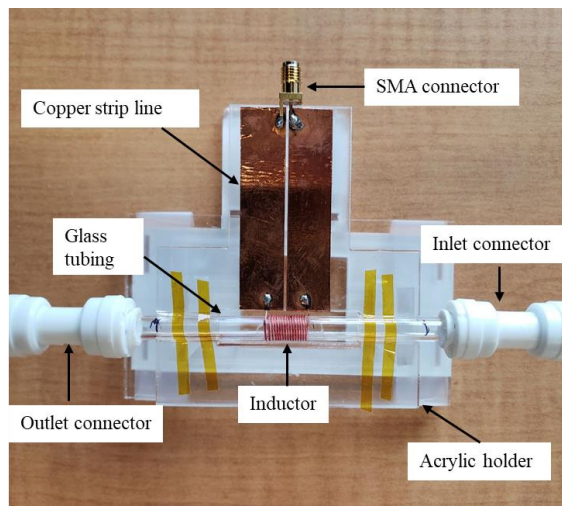


Figure 19. Top pictorial view of the sensor.

At the beginning of this project, we found that the response of our sensor was affected by noise from the environment. As we are working at microwave frequencies, signals from different sources such as various radio stations signals, local television channels signals, or microwave ovens signal can affect the measurement. To reduce the noise level from the environment, we used a “Faraday cage” as a solution to the noise problem. Figure 20 shows the top view of the device inside of the Faraday cage. The device is then connected to the vector network analyzer through the SMA connector and shown in Figure 21.

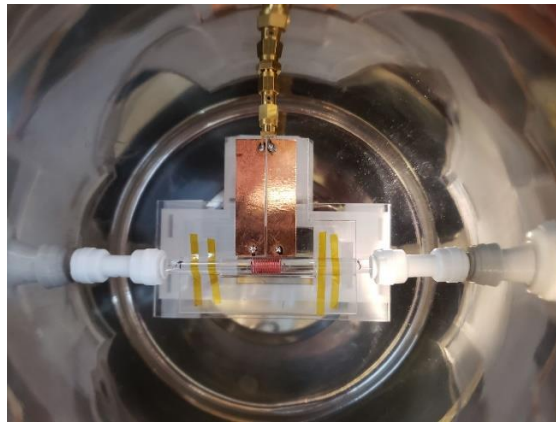


Figure 20. Top pictorial view of measurement set-up (inside Faraday cage).



Figure 21. Device connected with a vector network analyzer.

3.5 Solution preparation for NaCl and MgCl₂

In this project, the concentrations of sample solutions were prepared in terms of percent (%). In percent solution calculation, the amount (weight) of a solute (i.e. NaCl, MgCl₂) is expressed as a percentage of the total volume of solution. All the prepared solutions are expressed as weight/volume % (W/V %). Table 3-1 shows all the concentrations of prepared sample salt solutions (NaCl, MgCl₂) used for the experiments. Percentage solution equation:

$$\frac{\text{Weight}}{\text{Volume}} \% = \frac{\text{Weight of solute}}{\text{Volume of solution}} \times 100 \% \quad (58)$$

Example: To make 0.5% concentration of NaCl salt solution, 0.5 g of NaCl and 99.5 mL of water is used. The total weight is (99.5 + 0.5 = 100 g). For Pure water, 1g = 1mL.

This 100 mL solution will be divided into two 50 mL solutions; one 50 mL will be used to measure the S₁₁ response and the other 50 mL will be used as a seed to make diluted solutions. In this 50 mL seed solution, 50 mL of pure water is added to dilute the solution into lower concentration (half concentration of the seed solution concentration). Appropriate personal protective cloths and masks are used during solution preparation.

Example: To make 0.25% concentration of NaCl salt solution, 50 mL seed solution is used, and 50 mL pure water is added to that seed solution.

$$\text{Dilution equation: } C_1V_1 = C_2V_2 \quad (59)$$

Here,

C_1 = concentration of the stock solution

V_1 = volume from the stock

C_2 = final concentration of the diluted solution

V_2 = final volume of the diluted solution

Table 3-1. Concentrations of the sample salt solutions for NaCl and MgCl₂.

Concentrations of the salt solutions (NaCl, MgCl ₂) (ppm)
1000.0
500.0
100.0
50.0
25.0
12.5
6.0
3.0
1.5
0.8
0.4

3.6 Solution preparation of NaCl and MgCl₂ mix

To prepare the mix solution of NaCl and MgCl₂, the same amount of solid salt (NaCl and MgCl₂) is used. The process of mix solution preparation is described as an example. First, a NaCl solution of 0.01% and an MgCl₂ solution of 0.01% are prepared separately. To prepare a 0.01% solution, 0.02g of solid salt is dissolved into 200 mL of water. Then these separate 200 mL solutions are added together to make 0.01% of mixed (NaCl and MgCl₂) solution. So, the mix seed solution becomes 400mL of 0.01%. The dilution method described above is applied to generate the lower concentrations of the mixed solution. For example: to prepare 0.0025% mix solution, 600mL of pure DI water is added to the 200 mL of seed sample.

3.7 Vector Network Analyzer (VNA)

A vector network analyzer is an instrument that characterizes high-frequency passive and active devices and measures their effect on the amplitude and phase of swept-frequency and swept-power test signals.

A VNA generally includes four basic sections: sources for stimulus, signal-separation devices, and receivers that down-convert and detect the signals and processor/display for calculating and reviewing the results [34]. The signal source produces a stimulus for the device-under-test (DUT). The source can be used to sweep the frequency or sweep power levels of the signal. Open-loop voltage-controlled oscillators or synthesized sweepers are used to make the signal source. Figure 22 shows the generalized block diagram of a vector network analyzer.

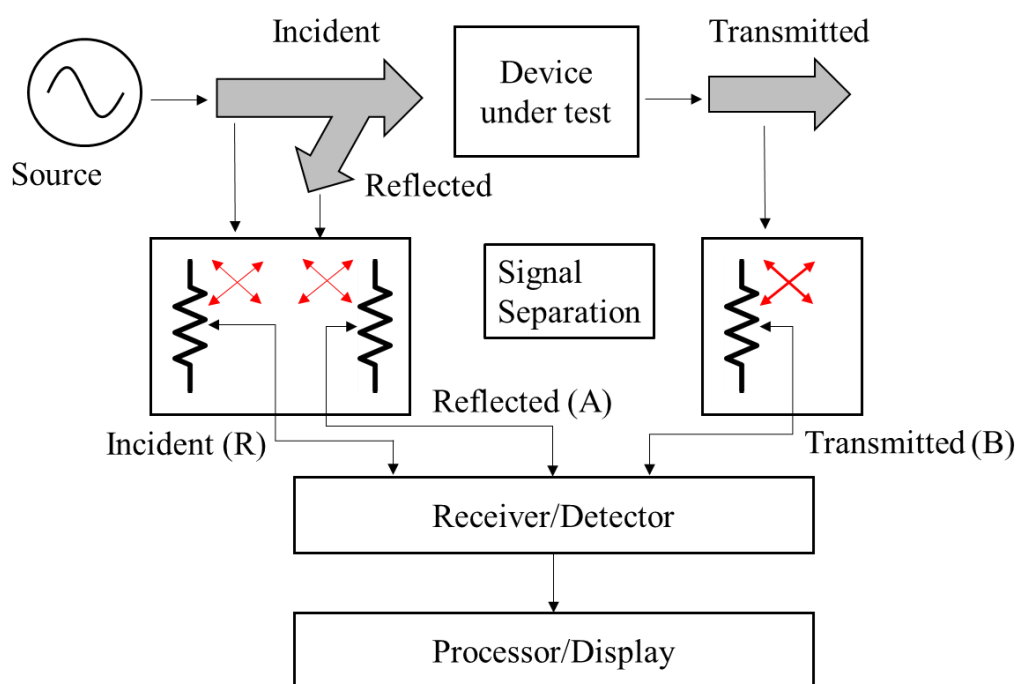


Figure 22. Generalized network analyzer block diagram [34].

Two major functions are performed by the signal separation block. First, it measures a portion of the incident signal using splitters or directional couplers. This data works as a reference to compute the ratio-based calculations. Second, the incident (forward) and reflected (reverse) traveling waves are separated at the input of the device under test (DUT) [34]. This job is done with couplers with excellent directivity performance. In addition to that, couplers are suitable as they have low loss and high reverse isolation properties. After this section, the signals enter the signal-detection block. The signal detection is performed using diode detectors and tuned receivers. Conversion of RF signals to proportional DC levels is done with diode detectors. In the receiver section, local oscillators are used to translate the signal to an intermediate frequency (IF) and this signal then passes through bandpass filters. After this section, the IF signal passes through an analog-to-digital converter and digital signal processing blocks to gather the magnitude and phase information. The output signal is then displayed in the monitor of the network analyzer. Figure 23 shows our vector network analyzer with two-port used in this project. The vector network analyzer (E8363B) is a product of Agilent Technology and it can operate within the frequency range of 10 MHz – 40 GHz.

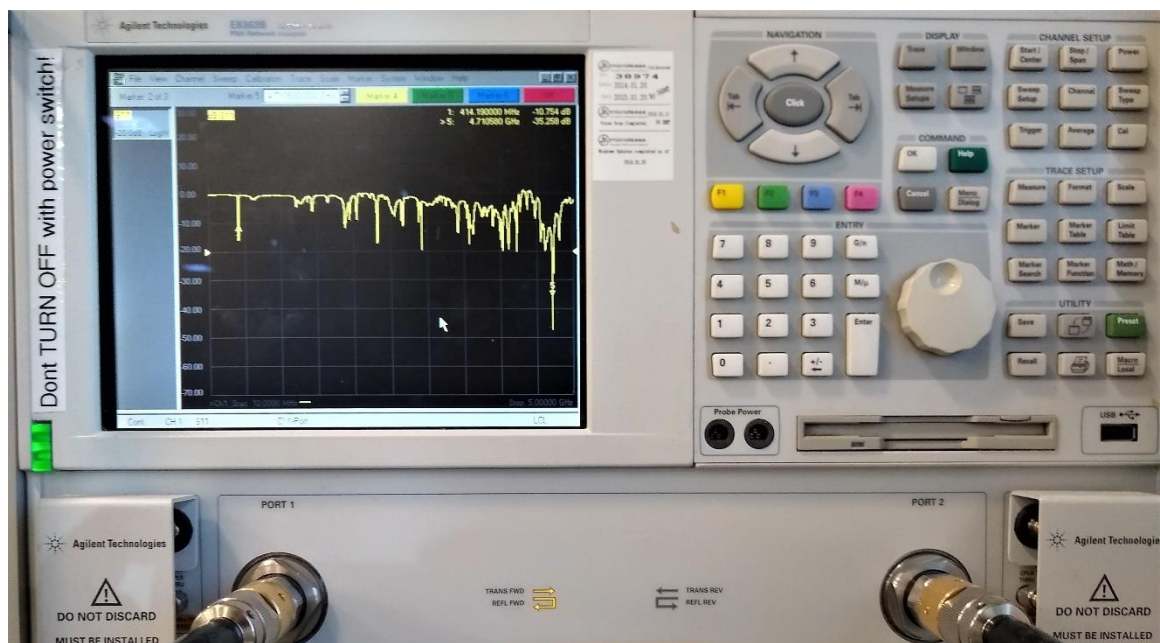


Figure 23. Vector Network Analyzer (VNA).

CHAPTER 4 MACHINE LEARNING ALGORITHM

4.1 Introduction

Machine learning is considered as a subset of artificial intelligence (AI) [41]. The term “Machine learning” refers to the recognition of patterns in a large number of data sets [42]. In a machine learning system, the machine learns without being explicitly programmed. Every time the machine encounters a change in the pattern, it tries to learn from that change and optimize its own code to the newly encountered scenarios. The learning of meaningful patterns includes specific tasks such as recognition, planning, control, prediction, etc.

Machine learning is a widely used technology and we use it every day in our day-to-day life. Uses of this technology include search engines that are programmed to learn to bring us the best results, anti-virus software, fraud detection while currency goes through transactions, detecting faces using personal assistance applications, visual tracking, object detection scanners and many more [43], [44]. Figure 24 shows the machine learning classification tree. Broadly, machine learning can be classified into supervised learning and unsupervised learning. In supervised learning, the model is developed based on the input and output data. In unsupervised learning, the grouping and interpretation of data are based on only the input data. Supervised learning is generally divided into two sections: classification and regression. Support vector regression is one part of the regression section. The clustering-based problems lie in the unsupervised learning section.

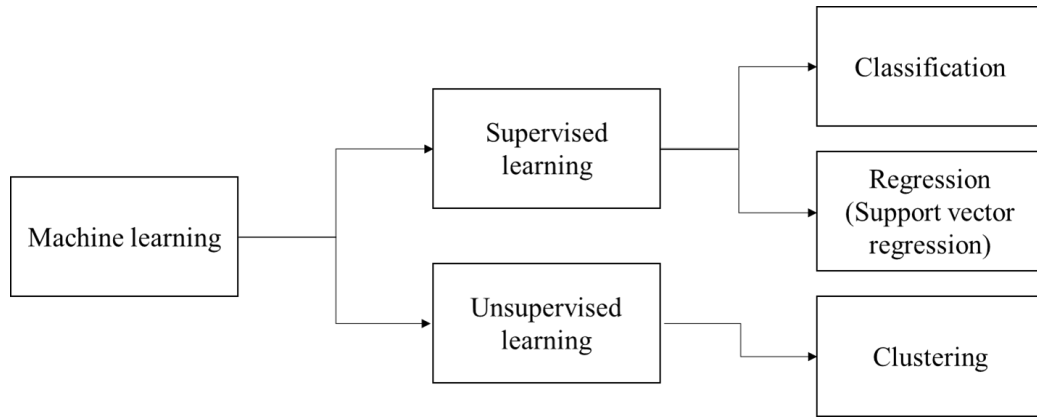


Figure 24. Machine learning classification.

4.2 Support vector regressor

Support vector regressor is a machine learning technique used for classification and regression process. It was first proposed by Vladimir Vapnik and his colleagues in 1992 at AT&T Bell Laboratories [45]. The initial focus of their work was optical character recognition (OCR), but soon support vector classifiers became popular for object detection problems. In the following section, some basic ideas about support vector machine are given.

Suppose, $\{(x_1, y_1), (x_2, y_2), \dots, (x_l, y_l)\} \subset \mathcal{X} \times \mathbb{R}$, where \mathcal{X} is the space of the input. According to Vapnik, 1995 [45], In a support vector (SV) regression model, we want to find a function $f(x)$ for all the training data. The function should have at a deviation, ε from the obtained targets y_i , so that the function can be valid for all the input data set. In this method, the error is not a first priority as long as it is less than ε but should not be larger than that. The linear function for the input can have the following form [42]:

$$f(x) = \langle w, x \rangle + b \text{ with } w \in \mathcal{X} \text{ and } b \in \mathbb{R} \quad (60)$$

In equation 60, $\langle w, x \rangle$ denotes the dot product in \mathcal{X} . By finding a small w , flatness is achieved. To obtain this condition, one way is to minimize the norm of w , i.e. $\|w\|^2 = \langle w, w \rangle$. The convex optimization form of this problem is [42]:

$$\begin{aligned} & \text{Minimize } \frac{1}{2} \|w\|^2 \\ & \text{Subject to } \begin{cases} y_i - \langle w, x_i \rangle - b \leq \varepsilon \\ \langle w, x_i \rangle + b - y_i \leq \varepsilon \end{cases} \end{aligned} \quad (61)$$

The assumption for equation 61 is such that for all pairs of (x_i, y_i) there exist a function $f(x)$ with ε precision.

But, depending on the point of interest, it may be necessary to accept some errors. In that case, we must consider the “soft margin” loss function that was introduced to the SV machine by Crotes and Vapnik, 1995 [42]. According to their theory, one can include slack variables ξ_i, ξ_i^* to the optimization problem. Therefore, the formulation becomes [42]:

$$\begin{aligned} & \text{Minimize } \frac{1}{2} \|w\|^2 + C \sum_{i=1}^l (\xi_i + \xi_i^*) \\ & \text{Subject to } \begin{cases} y_i - \langle w, x_i \rangle - b \leq \varepsilon + \xi_i \\ \langle w, x_i \rangle + b - y_i \leq \varepsilon + \xi_i^* \\ \xi_i, \xi_i^* \geq 0 \end{cases} \end{aligned} \quad (62)$$

Here, C is a constant and $C > 0$. C determines the offset between the flatness of function f and the amount up to which deviations larger than ε are tolerated. So, we can describe the loss function $|\xi|_\varepsilon$ as explained in equation 63. This situation is shown in Figure 25.

$$|\xi|_\varepsilon = \begin{cases} 0 & \text{if } |\xi| \leq \varepsilon \\ |\xi| - \varepsilon & \text{otherwise} \end{cases} \quad (63)$$

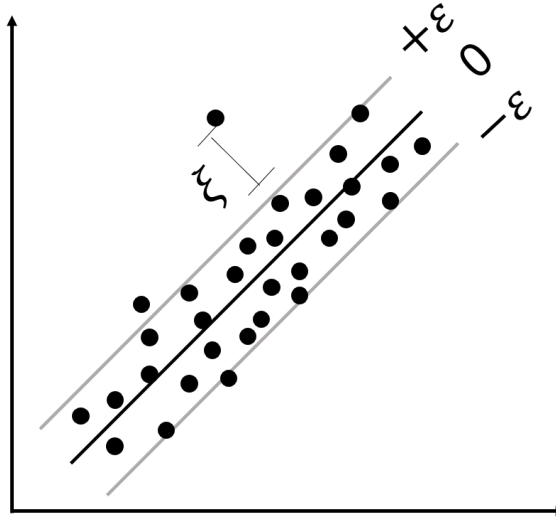


Figure 25. Soft margin loss setting for a linear support vector regressor [42].

In this project, we introduce the machine learning approach to identify different salt components and their concentration. This approach includes training a support vector regressor (SVR) using MATLAB.

4.3 Linear support vector machine regression model

In MATLAB, there are several built-in SVR models. We use the “fitrsvm” model. This model supports mapping with lower through moderate-dimensional predictor data set using kernel functions. Based on the data sets, it trains and cross-validates a support vector regression model. The usual syntax for fitrsvm is [46]:

$$Mdl = \text{fitrsvm}(X, Y)$$

This model (Mdl) trains the SVR with input matrix X and returns the response as vector Y.

In this project, the measured reflection coefficient (S_{11}) data is the input data set. The data set includes 20,000 amplitude and 20,000 phase values as the input matrix. The phase values are unwrapped using the “unwrap” function from MATLAB. All the input data is normalized to [0, 1]. Depending on the application, we can train the model once and test the element of interest or we can train each time before testing.

The regressor model includes cross-validation of two support vector machine (SVM) regression models using 10-fold cross-validation method. The model is specified to train using the default linear kernel model.

$$Mdl = fitrsvm(X, Y, 'Kfold', 10)$$

4.4 Optimize SVM Regression

In this project, the code required optimization for precise training and prediction. MATLAB has several built-in optimization functions. This section explains those functions that we used in our code.

The eligible parameters for the `fitrsvm` are ‘BoxConstraint’, ‘KernelScale’, ‘Epsilon’, ‘KernelFunction’, ‘PolynomialOrder’, and ‘Standardize’. By setting ‘all’, we considered all possible eligible parameters for optimizing the SVM regression. For further improvement, the code modifies the effect of the ‘OptimizeHyperparameters’ function using the ‘HyperparameterOptimizationOptions’ function [46]. Table 4-1 shows the functions used in the code to train and predict.

Table 4-1. Hyperparameter optimization functions for SVR model.

Field name	Description	Syntax
K-fold	In the K-fold cross-validation method, k-1 folds are used for training and the last fold is used for evaluation. This process is repeated k-1 times, leaving one different fold for evaluation each time. In our code, nine folds are used for training and one fold for evaluation.	<i>'kfold', 10</i>
Verbose	'Verbose' defines the verbosity level. It can have 0, 1 or 2 values. 0 defines no iterative display, 1 defines the iterative display and 2 defines iterative display with extra information. In our code, we used 0.	<i>Verbose', 0</i>
MaxObjectiveEvaluations	It is defined as the maximum number of objective function evaluations. For our code, this value is set to 20.	<i>'MaxObjective Evaluations', 20</i>
CacheSize	The allocated memory size that is reserved for the entire n-by-n matrix is defined as 'CacheSize'. In this code, CacheSize is maximal, so that the software can reserve enough memory space to hold and evaluate the entire matrix.	<i>'CacheSize', 'maximal</i>
Gaptolerance	'Gaptolerance' is used to check the convergence. In this code, the 'Gaptolerance' is set to 0 that means, convergence will not be checked by the fitrsvm model using this parameter.	<i>'GapTolerance', 0</i>
Yfit	Once the model is trained, it is used to test the examined data set. 'Yfit' is used to predict the data set.	<i>Yfit = predict(Mdl, X)</i>

4.5 Flowchart of the SVR algorithm

The SVR method establishes a regression hyperplane using the training data and based on that hyperplane, it tries to predict the test data. Figure 26 shows the flowchart of

the machine learning algorithm. The algorithm includes three stages: an input stage, training stage, and testing stage.

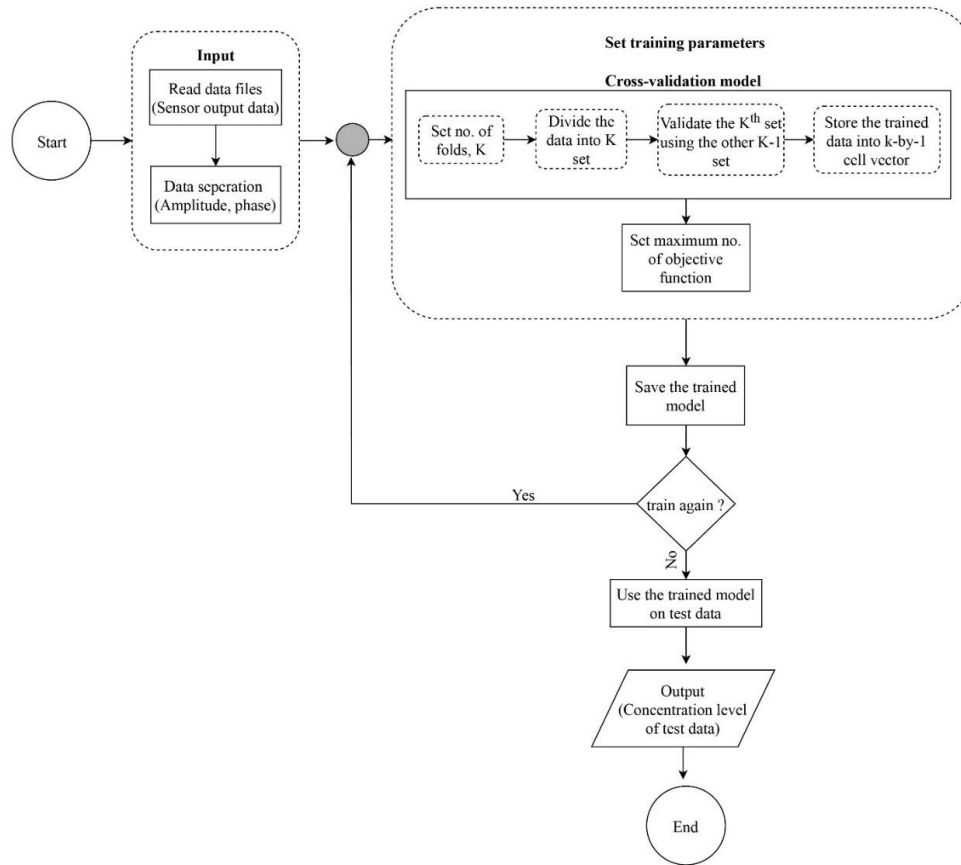
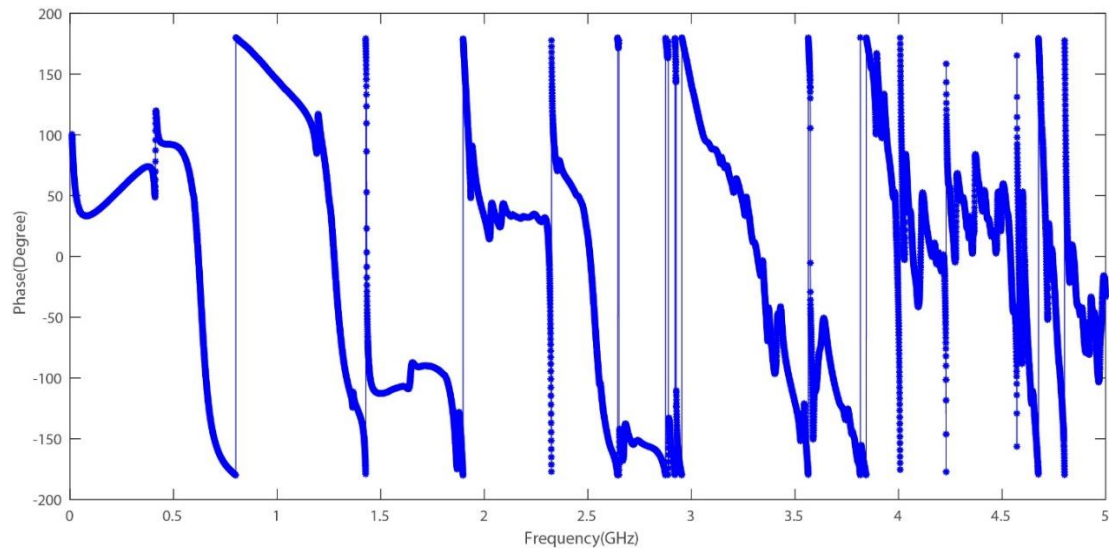


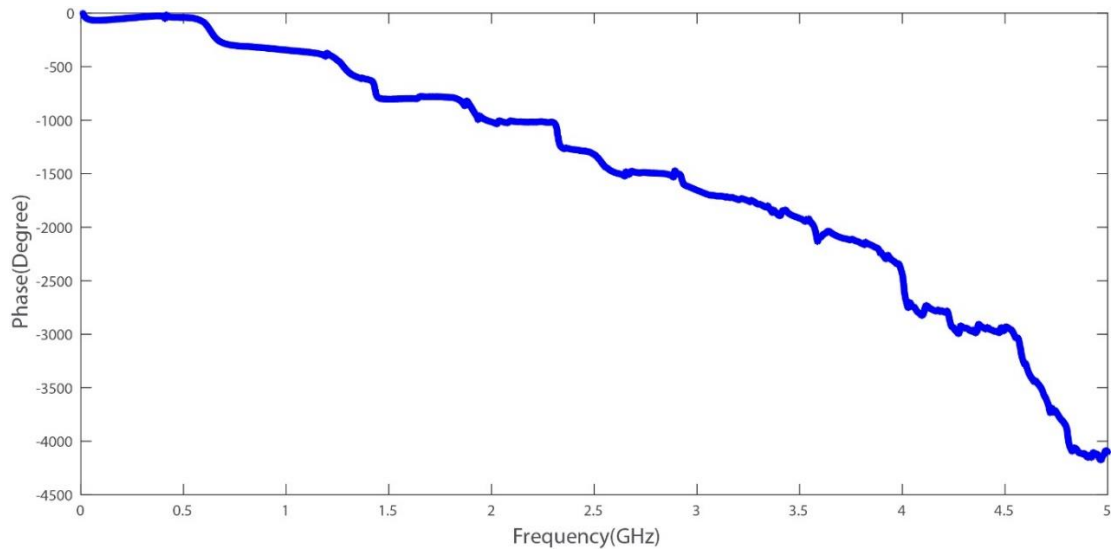
Figure 26. Flowchart of the machine learning algorithm.

Input stage: The measured reflection coefficient (S_{11}) data are the input files in this project. The algorithm first reads all the data files. Then, the algorithm separates the amplitude and phase from the text files and uses them as the training data. The unwrap function is used for the phase values. Figure 27 shows the unwrapped and wrapped phase of input data. If there exist absolute jumps between successive features of phase that are greater than or equal to the default jump tolerance of π radians, the unwrap function

corrects the phase angle by adding multiples of $\pm 2\pi$ of the radian phase angles in a vector [47].



(a)



(b)

Figure 27. Phase (a) wrapped and (b) unwrapped.

Training stage: In the training stage, a cross-validate SVM regression model is trained. The model is optimized with different hyperparameter functions. The k-fold

validation method is used for the cross-validation. The average root-mean-square-error between the predicted concentrations and their actual values are very small. Figure 28 shows minimum objectives vs. the number of function evaluations from the MATLAB operation. The figure represents the optimization of a cross-validated SVR using bayesopt to minimize the cross-validation loss. The trained model is saved and used for the test purpose.

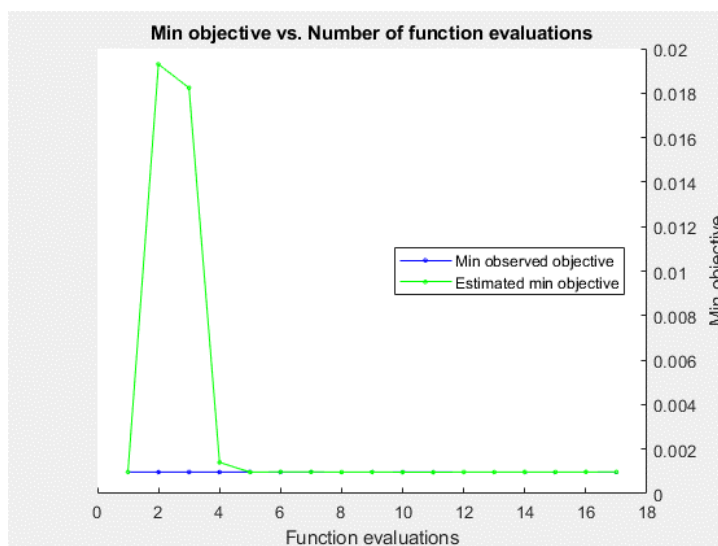


Figure 28. Min objective vs. Number of function evaluations.

Testing stage: The trained model is used to predict the concentration of the test data. Based on the trained regression model, a vector of predicted responses for the predictor data is obtained. From the error calculation, we can determine how well the model is able to predict different concentrations of the tested data.

4.6 Concentration prediction using support vector regressors

In this project, a support vector regressor (SVR) is trained using the collected data set for different concentration of each element. The collected data sample concentrations for NaCl and MgCl₂ are mentioned in Table 3.1. For mix solution of NaCl and MgCl₂, the experiment was performed with concentrations of 0.01%, 0.0025%, 0.000625%, 0.00015625%, and 0.000039062%. All the concentrations are converted into parts per million (ppm) unit respectively when they are presented into figures. Fifteen samples were collected for each concentration value. The liquid samples stayed inside of the sensor tube for 24 hours and the sampled data are collected every hour.

The training data is constructed by concatenating the 20,000 amplitudes and 20,000 phase values of the frequency response measured by the sensor. So, the final input vectors have 40,000 dimensions. The output of this algorithm is presented in the result section of chapter five. The results indicate that the SVR is able to predict the concentrations of the samples with high accuracy.

4.7 Visualization of the SVR model result

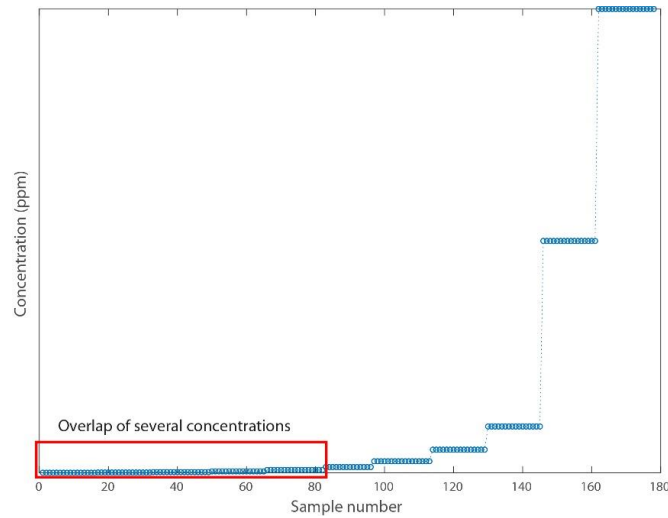


Figure 29. Prediction problem for lower concentration.

As there exists a wide range of concentrations, it was difficult for the model to distinguish the lower concentrations precisely. Figure 29 shows that all the lower concentrations merged together and are hard to distinguish. This problem was solved by converting the “labels” to a log scale. The conversion solved the problem for predicting the lower concentrations more precisely with lower root-mean-square error (RMSE). Figure 30 shows the result after taking the log scale.

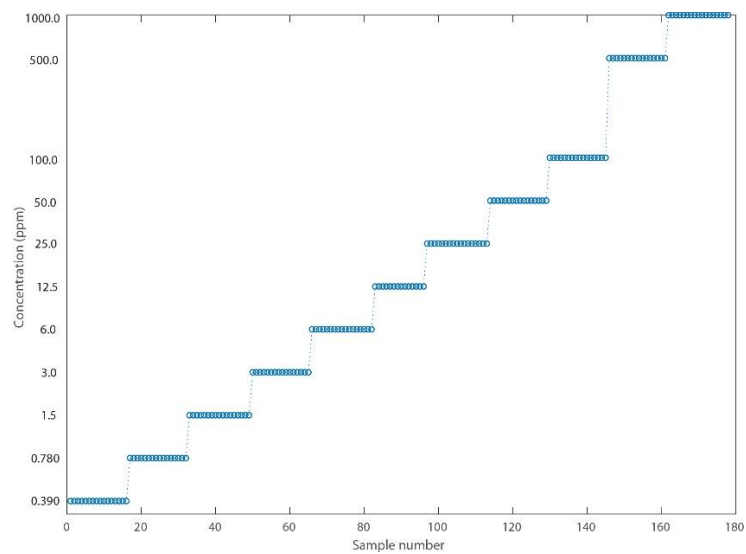


Figure 30. Improved visualization with a log scale.

CHAPTER 5 EXPERIMENTAL RESULTS AND DISCUSSION

This chapter contains the experimental results and discussion of this project. At the beginning of this chapter, the optimization of the sensor is presented. The sensor is optimized based on the number of turns in a coil and the effect of static magnets on the amplitude and phase response of the sensor. After that, two different approaches to detect contaminants are presented for NaCl, MgCl₂, and, mix solution (NaCl + MgCl₂). The first approach is the direct measurement of the reflection coefficient method and the second approach is a machine learning method.

5.1 Optimization of the sensor

The objective of this project is to detect some specific water contaminants (Na and Mg). A novel technology is introduced that can detect water contaminants continuously in real-time. In this section, the optimization of the sensor is presented. As our sensor is an inductive sensor, the optimization is based on the number of turns in the coil. To reduce parasitic effects and achieve the maximum sensitivity of the sensor, the spacing between successive turns of the coil is set equal to the diameter of the wire.

5.1.1 Optimization of the sensor for coils with different number of turns

To optimize the sensitivity of our sensor, we tried 3 coils with a different number of turns: 16 turns, 29 turns, and 42 turns. Figure 31 shows the pictorial view of three sensors with a different number of turns.

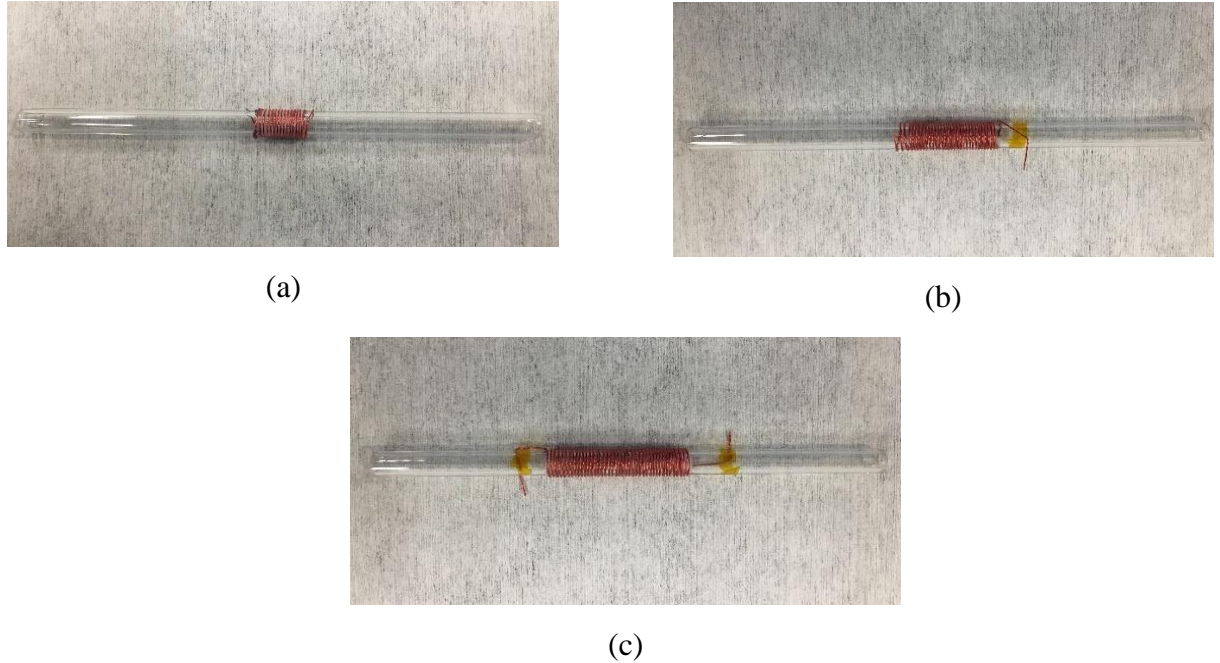


Figure 31. Coils with different turns (a) 16 turns (b) 29 turns (c) 42 turns.

We measured the reflection coefficient (S_{11}) for all three sensors and the results are shown in Figures 32, 33, and 34 for 16 turns, 29 turns, and 42 turns respectively. The experiment was performed with three different materials: air, DI water, and 1% NaCl salt solution. The operating frequency range for each experiment was 10 MHz – 3 GHz. All the reflection coefficient graphs include two results: the top section is the amplitude response and the bottom section is the phase response. For both sections, the x-axis is labeled as the frequency in GHz unit and the y-axis shows S_{11} in dB for amplitude response and phase in degree.

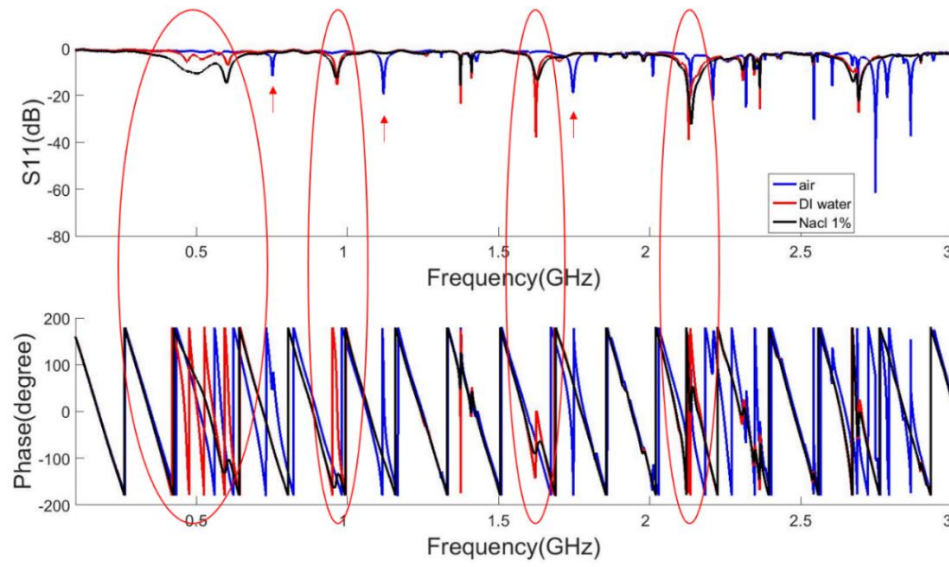


Figure 32. Reflection coefficient (S_{11}) response with 16 turns coil.

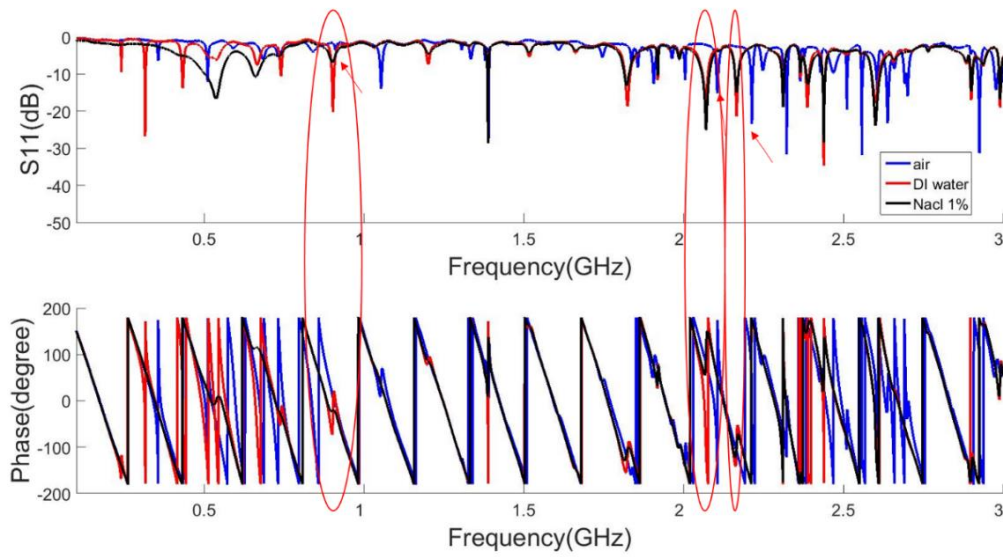


Figure 33. Reflection coefficient (S_{11}) response with 29 turns coil.

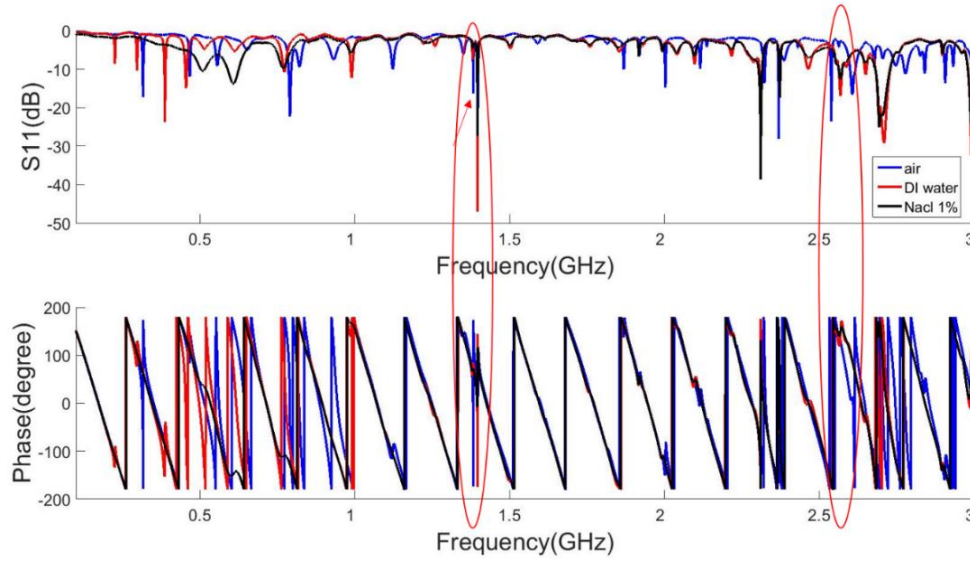


Figure 34. Reflection coefficient (S_{11}) response with 42 turns coil.

To analyze the results for all three different sensors, we fixed four selection rules.

The selection rules will allow us to monitor the resonances for some specific frequency ranges. The selection rules are given below.

Selection rules:

1. Resonances
2. Looking for a difference between air and liquid
3. Looking for a similar pattern between liquids
4. Distinct amplitudes and Q factors

In the experimental results, we are looking for the resonances and respective phase response for all three different materials. Different materials act as different mediums. When the signal is applied through the sensor, the applied fields begin to alternate in polarity which causes a response in the material. The response depends on the

permittivity, permeability, and conductivity of the material. As a result of changing conductivity, heating of the material may occur which requires absorbing energy from the input signal. Thus, the reflected signal will be smaller than the incident signal, and the response will be noticed in the reflection coefficient (S_{11}) measurement. With more absorption of energy, the reflection coefficient value will be lower and the peaks will be more prominent. This indicates that the medium attains its most lossy state at the resonant frequency of the coil. In general, for a particular material, there can exist several natural frequencies [37]. If the medium possesses multiple resonant frequencies, multiple variations in amplitude and phase would be observed in different frequencies in a given frequency spectrum. That is why in the amplitude response of the reflection coefficient measurement, we observe multiple down peaks at different frequencies.

At a certain frequency, the resonant peaks for the air and liquid should be different as they are a different state of the material. Based on this point, we selected our second selection rule. The air and liquid may have resonance peaks at different frequencies. This is also observed in the response of reflection coefficient graph. In the indicated red circular sections, it is observed that the response from air and liquid are different in both amplitude and phase.

The response from DI water and the salt solution can have resonance peaks at similar frequencies, as both materials are in the liquid state. Based on this point, the third rule is selected. Similar responses can be observed for them. However, there must exist some unique frequencies where only the NaCl salt solution has resonance peaks. The fourth selection rule is based on the distinct amplitude and quality factor or Q-value. As

there are multiple resonance peaks, we are looking for those frequencies, where sharp down peaks are observed.

Based on the above-mentioned rules, we have selected some frequency ranges. Within those ranges, the responses follow all four selection rules. The selected frequency ranges are marked with the red circle in Figures 32, 33, and 34. For 16 turn coil, we found 4 different ranges, for 29 turns we found 3 ranges and for 42 turns we found 2 different ranges to monitor the response. We selected the 16 turn coil as our optimized sensor for this project as it showed a more selective and highly sensitive response to different materials. The rest of the experiments in this project are performed with the 16 turn coil.

5.1.2 Optimization of the sensor with and without static magnet

In this project, the effect of the permanent magnet is observed on the S_{11} measurement of different liquid solutions. Figure 35 shows the static magnet and device holder. Two static magnets each with one Tesla magnetic flux density are used as permanent magnets. The magnets were bought from “SUPERMAGNET MAN” company. The static magnets may increase the magnetic field strength that may affect the response of the ion to the applied signals. The magnets are placed outside of the inductor. A device holder is made with a 3-D printer machine to hold the sensor and the static magnets.

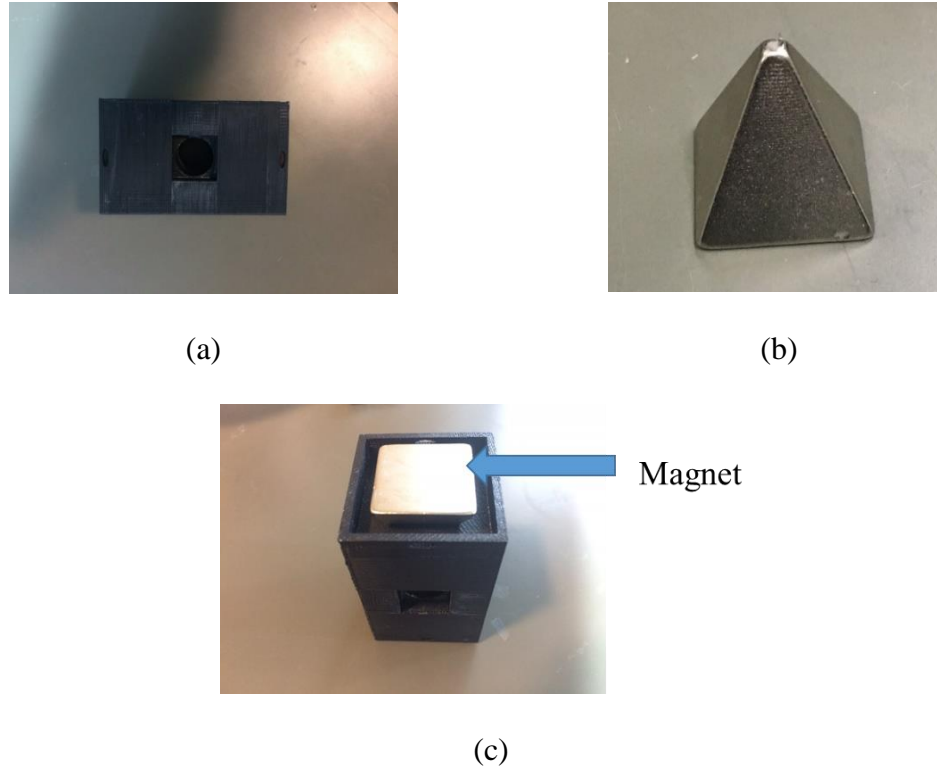


Figure 35. (a) Device holder (b) Static magnet (c) Device holder with magnet.

Figures 36 and 37 show the S_{11} measurement with and without magnets with 16 turns of the inductor coil. The magnets are introduced to find out how the strong magnetic fields from the static magnets may affect the reflection coefficient result.

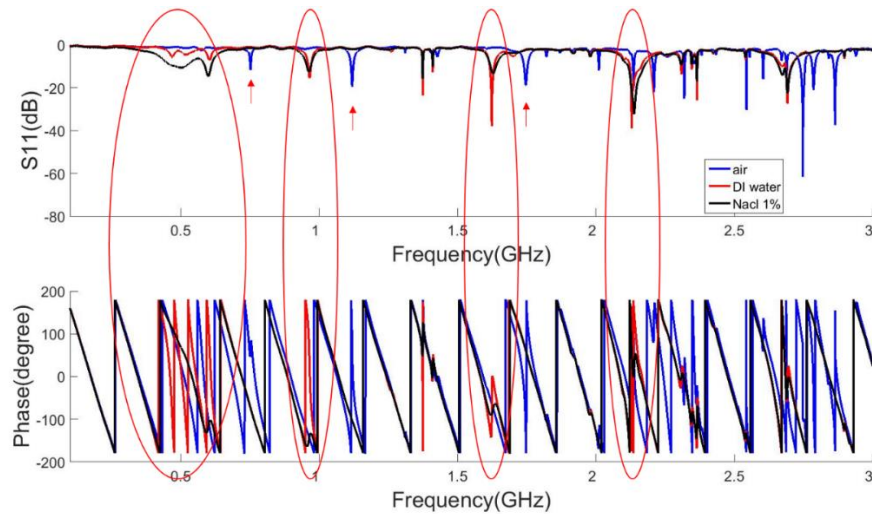


Figure 36. Reflection coefficient S_{11} measurement without the magnets.

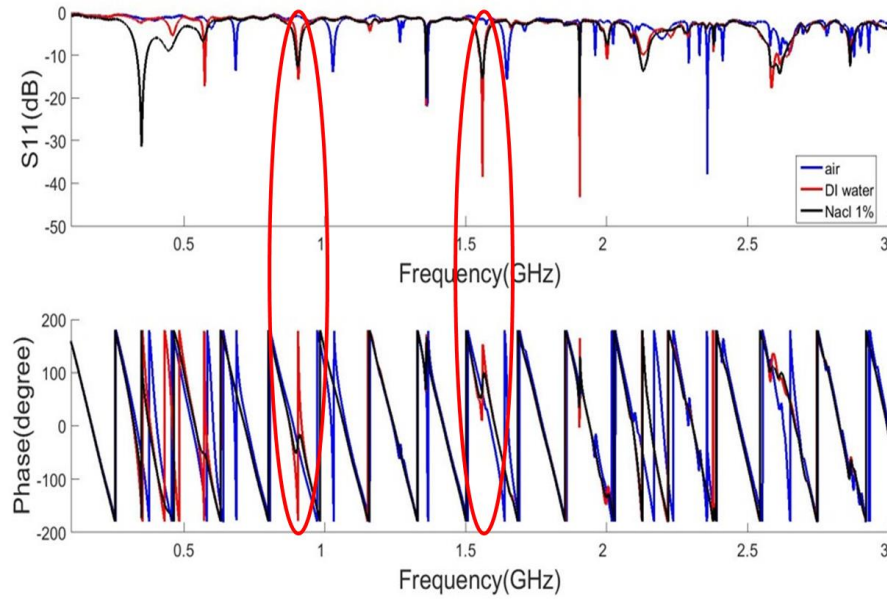


Figure 37. Reflection coefficient S_{11} measurement with the magnets.

Using the selection rule mentioned in the previous section, we selected the red circled frequency ranges to observe the effect of static magnets. After analyzing the results, it was found that with the static magnets, only the amplitude response is amplified by a small amount and no noticeable frequency shifts were observed. Thus, we decided not to use the magnets for further experiments. After several experiments for optimization of the device, the final device is fixed as a 16-turn coil and without the magnets.

5.2 Issues related to analyzing the reflection coefficient measurement

Our first approach was to measure the reflection coefficient (S_{11}) as a function of frequency. It is observed that, in the entire spectrum (10 MHz – 3 GHz), there are more

than 25 peaks and it is difficult for the human eye to monitor the frequency shifts and amplitude changes for all these peaks continuously in real-time. As a solution to this problem, we introduced machine learning to analyze the measured data from the reflection coefficient measurement. In the machine learning method, we increased the frequency range from 3 GHz to 5 GHz, to increase the input data set. The machine learning algorithm is entirely based on the measured data, thus increased frequency range will improve the concentration prediction. In the next section, experimental results for sodium chloride (NaCl), magnesium chloride (MgCl_2) and their mixture solution (NaCl + MgCl_2) are presented.

5.3 Experimental results for sodium chloride (NaCl) salt solutions

5.3.1 Reflection coefficient measurement

With the optimized sensor, we measured reflection coefficient of sodium chloride (NaCl) salt solutions. We performed the experiments with the different concentrations of salt solutions and the concentrations are presented in Table 3-1. Figure 38 shows the reflection coefficient response for different concentrations of NaCl salt solutions. All the solutions were prepared using the weighted concentration method and preparation method presented in chapter three. With these solutions, the reflection coefficient (S_{11}) is measured within the frequency range from 10 MHz – 5 GHz.

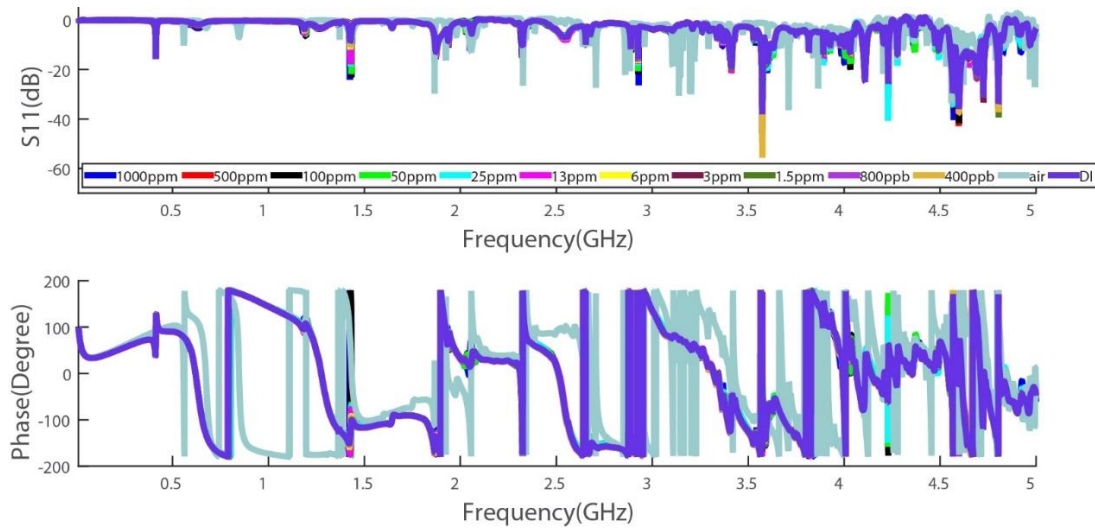


Figure 38. Reflection coefficient (S_{11}) response of NaCl salt solutions for different concentrations.

As the entire frequency spectrum is presented in one graph, it is difficult to identify the resonance peaks for different concentrations. If we magnify a certain frequency range, we can visualize the responses more clearly. Figure 39 shows the magnified response for all the measured concentrations of NaCl from 400 MHz – 430 MHz. The principal resonance frequency for NaCl is at 413.9 MHz. At that frequency, the lower the concentration gets, the more the energy is absorbed and thus, the reflection becomes smaller.

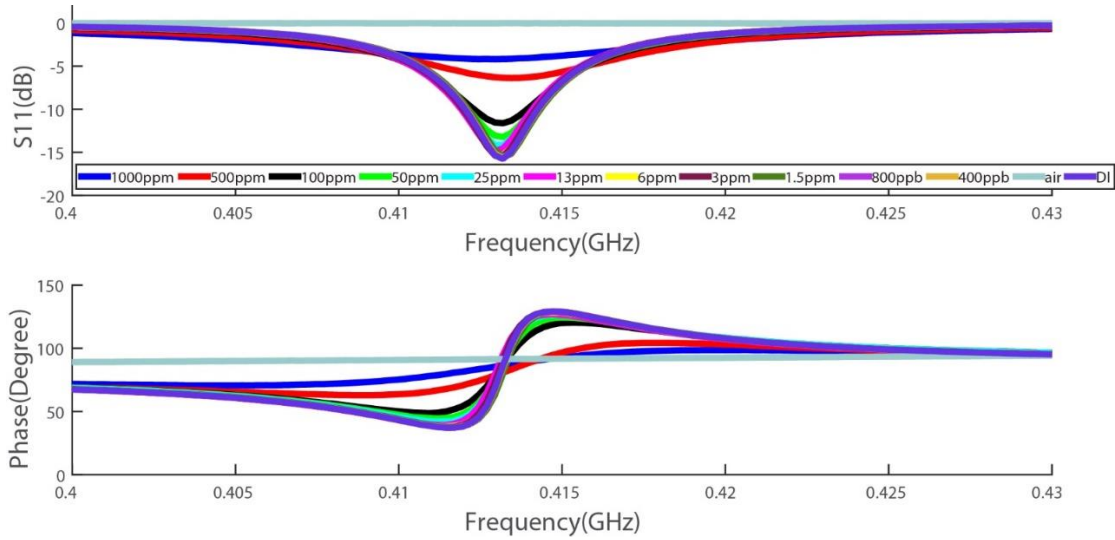


Figure 39. Reflection coefficient (S_{11}) response of NaCl salt solution for different concentrations at 413.9 MHz.

5.3.2 Machine learning approach

The measured reflection coefficient data for the different concentrations of NaCl salt solutions are given as input data to the algorithm. The algorithm creates a trained model based on the amplitude and phase response from the input data. The trained model is then used to predict the concentrations of the test samples. Figures 40 to 43 show the results for 1000 ppm, 100 ppm, 6 ppm and, 400 ppb and 800 ppb respectively using the machine learning approach. In these figures, the x-axis is labeled with the sample number, which represents the number of text files from the reflection coefficient measurement given as input data. The y-axis is labeled as the concentration with parts per million (ppm) unit. Although the solutions were prepared in percent (%) as concentration unit, all the (%) concentrations are converted to ppm unit respectively when presented in the figures. In these figures, the blue circles (o) represent the text files (each text file represents 40K point measurement) given as input data for the trained model. Each blue

circle represents one text file. The model is trained with different concentrations. The red asterisks (*) represents text files whose concentrations are predicted. In Figure 40, the model is trained with 25 ppm, 50 ppm, 100 ppm, 500 ppm, and 1,000 ppm concentrations and then, the model is asked to predict the concentrations of the text files marked with an asterisk (*). The actual concentration of the tested samples is 1,000 ppm and based on the output result shown in Figure 40, it can be said that the model is trained well to predict the tested concentration with high accuracy.

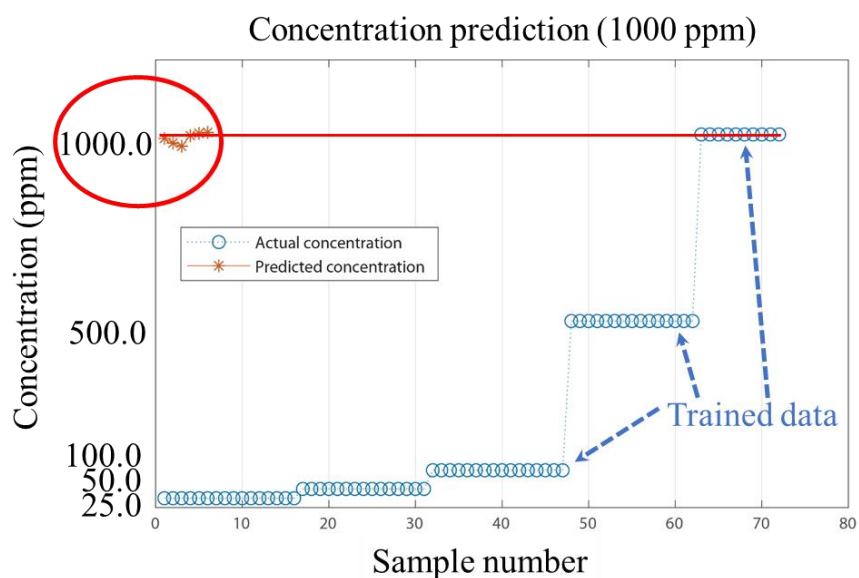


Figure 40. Concentration prediction of NaCl salt solution (1000 ppm).

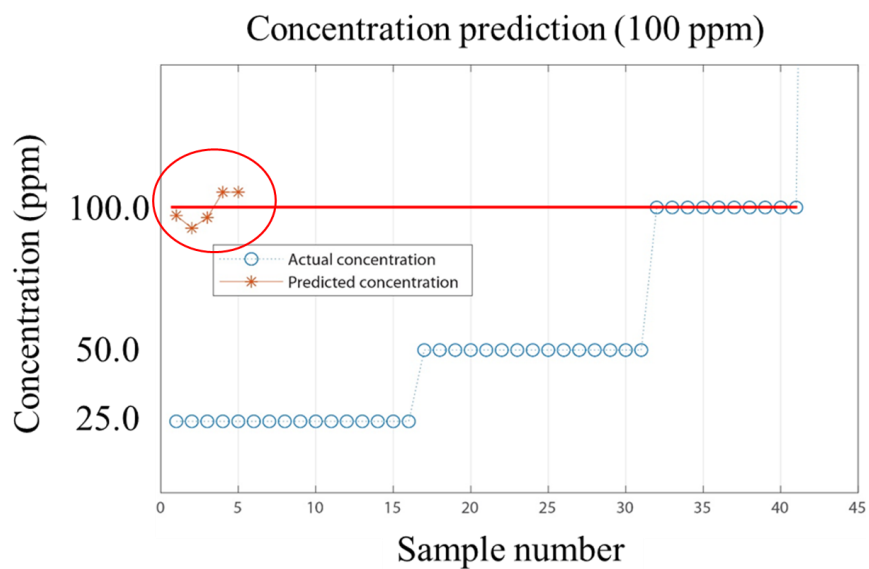


Figure 41. Concentration prediction of NaCl salt solution (100 ppm).

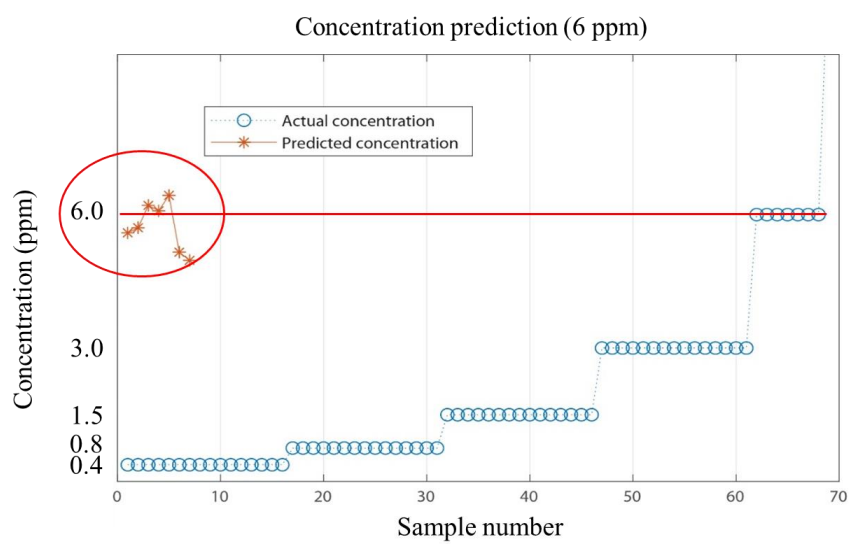


Figure 42. Concentration prediction of NaCl salt solution (6 ppm).

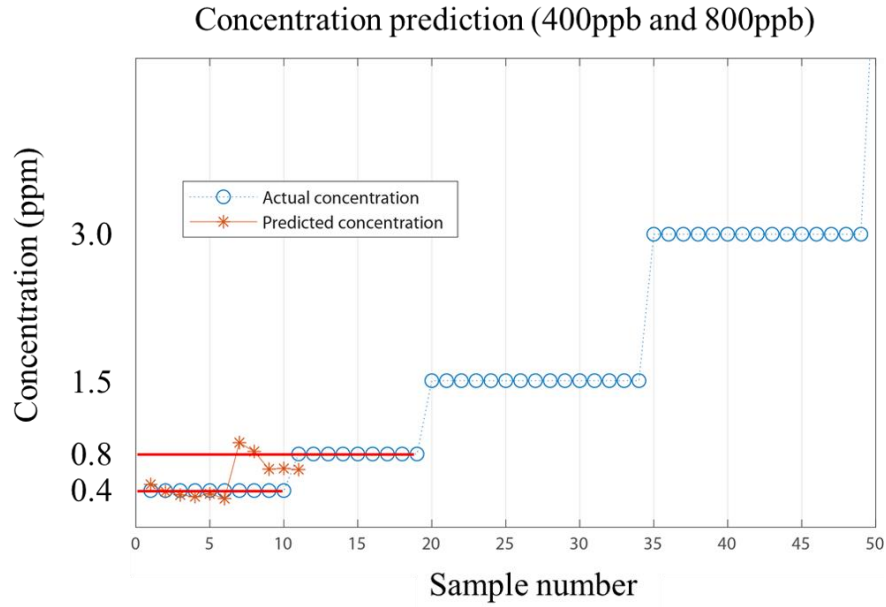


Figure 43. Concentration prediction of NaCl salt solution (400 ppb and 800 ppb).

5.3.3 Standard deviation calculation for different concentrations of NaCl

Figure 44 shows the standard deviation result of the measured data for all the concentrations of NaCl salt solutions. The x-axis is labeled with different NaCl concentrations with ppm unit and the y-axis is labeled with standard deviation value. The central box represents the central 50% of the data and the red line inside each box represents the median of the data. The red + signs are the outliers of the input data set. Normalized amplitude and phase measured data is considered as input data. The boxplot result indicates that the difference among different quartile with respect to the median is not equal for each concentration and some outliers also exist in the measurement.

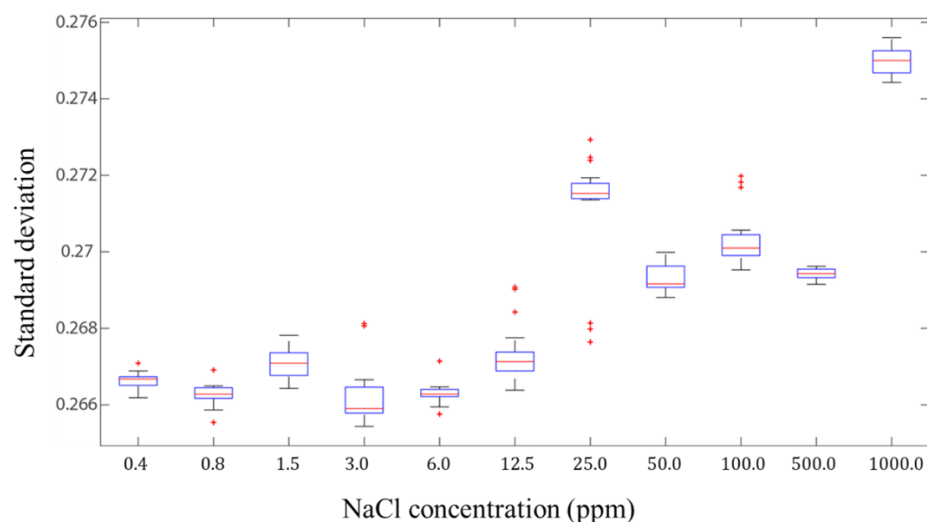


Figure 44. Standard deviation of measured data for different concentrations of NaCl solutions.

The outliers in the measured data may add additional error in the concentration prediction calculation. To optimize the data selection process and improve the performance of the SVR model, the outliers are identified and removed from the input data sets. Figure 45 shows the standard deviation of different NaCl concentrations with outliers removed from the red circled concentrations. The outliers are removed from 100 ppm, 6 ppm, 0.8 ppm, and 0.4 ppm concentrations. However, outliers still exist for 6 ppm and 0.8 ppm data files after the removal of specific data files that were calculated as outliers in the first standard deviation calculation.

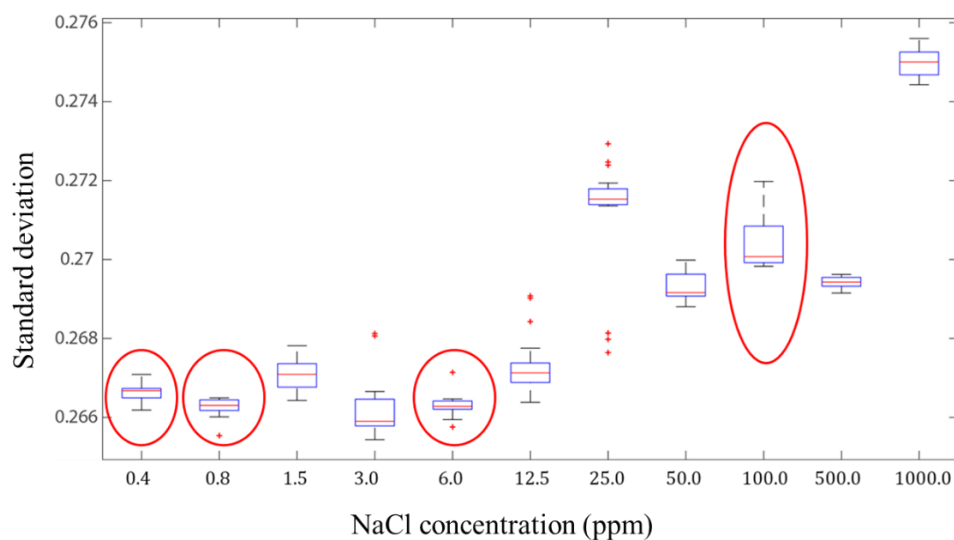
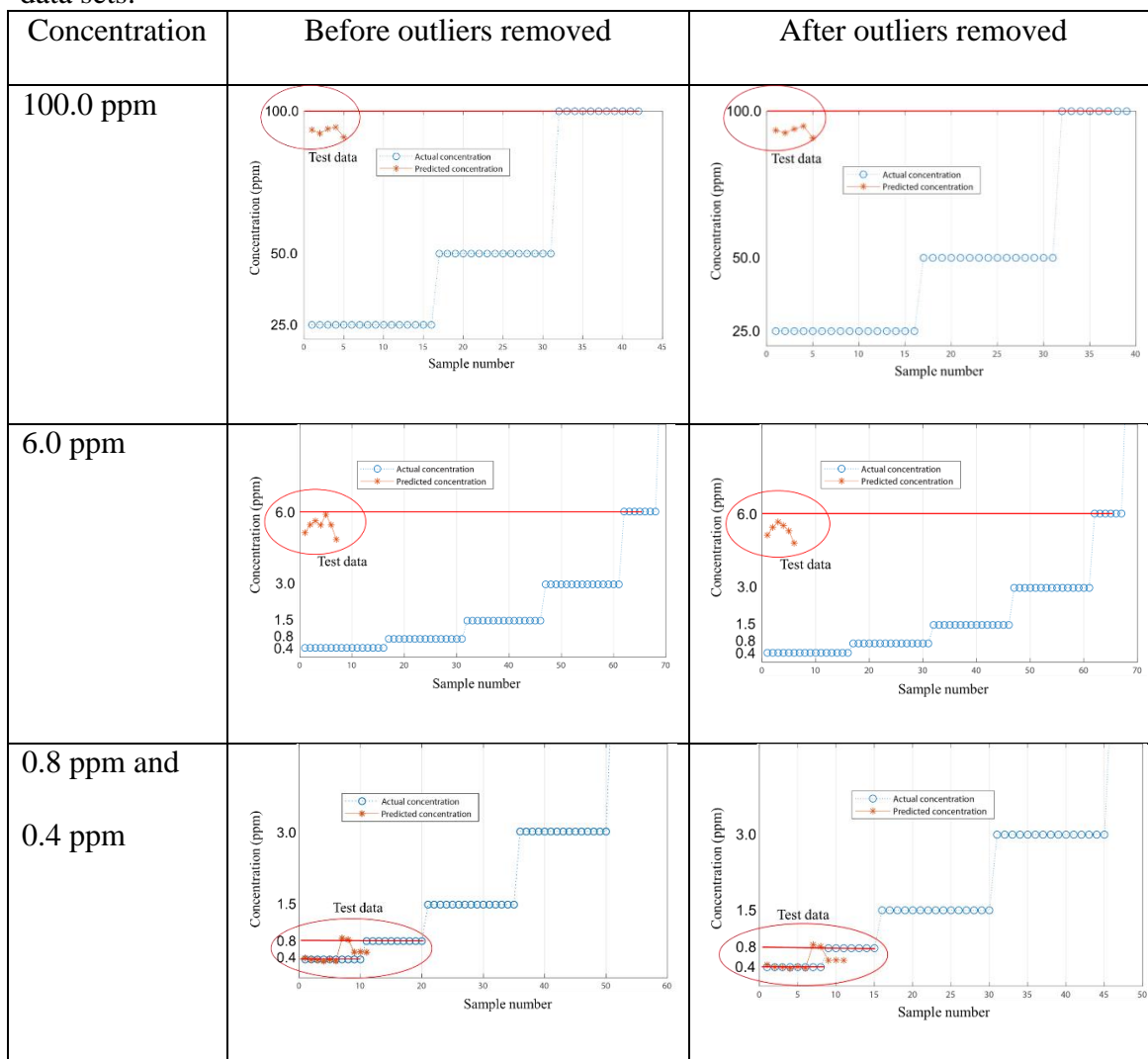


Figure 45. Standard deviation of measured data for different concentrations of NaCl solutions with outliers removed from red circled concentrations.

After the outlier files are removed, the remaining data sets are used as input data and we applied the machine learning approach to predict the concentrations. Table 5-1 shows the prediction results for 100 ppm, 6 ppm, 0.8 ppm, and 0.4 ppm concentrations. The results indicate that the removal of outliers file increased the accuracy of concentration prediction for 6 ppm. However, for the other concentrations (100 ppm, 0.8 ppm, and 0.4 ppm) significant improvement for concentration prediction is not noticed.

Table 5-1 Concentration prediction result after the outliers are removed from the input data sets.



5.3.4 Conductivity measurement for different concentrations of NaCl

Conductivity, temperature, and pH can be considered as potential variables that may affect the reflection coefficient measurement. Thus, these variables have been recorded during the experiments. Figure 46 shows a picture of an ultrameter manufactured by Myron L. This device is used to measure the conductivity, temperature,

and pH of the tested salt solutions. The temperature of the test environment during the experiment was recorded from 17 °C – 23 °C. The pH of different concentrations of NaCl was 5.2 – 5.7.



Figure 46. Ultrameter device to measure conductivity, temperature, and pH.

We have also measured the conductivity for different concentrations of NaCl.

Figure 47 shows the conductivity measurement for NaCl salt solutions. In this figure, the y-axis label is the conductivity in micro-siemens/cm unit and concentration in ppm unit is shown in the x-axis. For higher concentrations (1000 ppm – 6 ppm), the curve is found to be more linear than for the lower concentrations (6 ppm – 400 ppb).

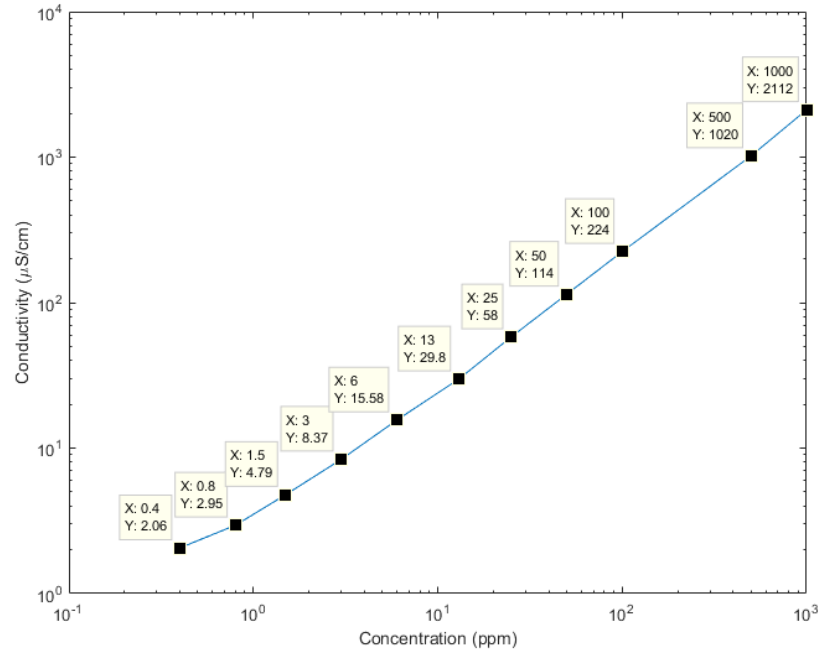


Figure 47. NaCl conductivity measurement for different concentrations of salt solution.

5.4 Experimental results for magnesium chloride (MgCl_2) salt solutions

In this section, experimental results with magnesium chloride (MgCl_2) are presented. Figure 48 shows the reflection coefficient (S_{11}) measurement for MgCl_2 . We have considered the same 11 different concentrations for MgCl_2 shown in Table 3.1. Different materials will have resonance peaks at different frequencies, thus, the resonance peaks of MgCl_2 are observed at different frequencies than those of NaCl.

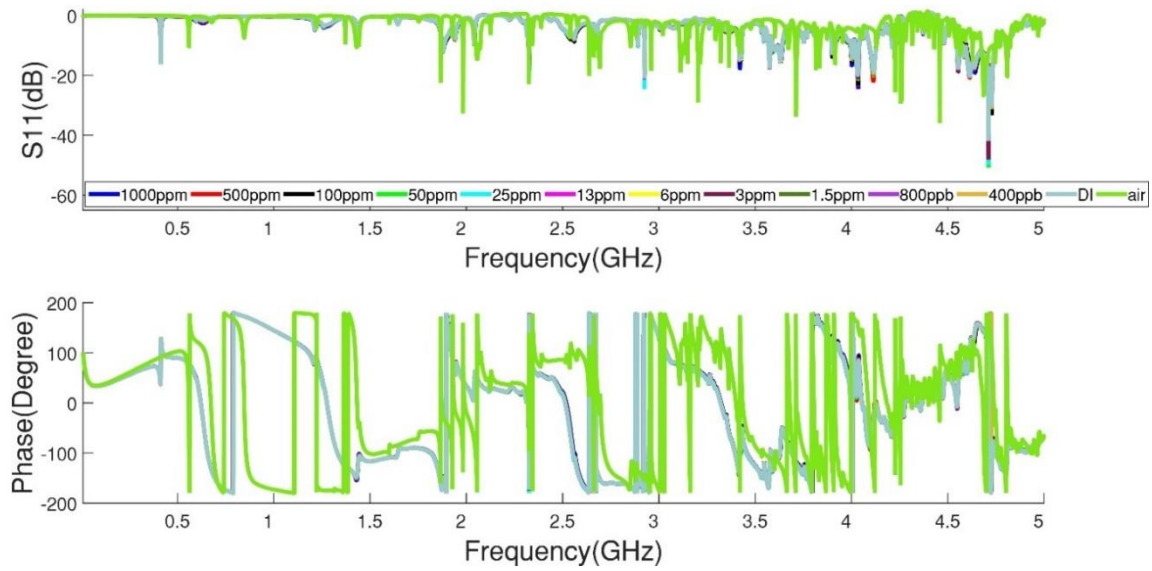


Figure 48. Reflection coefficient (S_{11}) response of $MgCl_2$ salt solutions for different concentrations.

For $MgCl_2$, we have also applied the machine learning approach. The training and testing approaches are the same as for $NaCl$. For $MgCl_2$, we have divided the 11 different concentrations into two groups: high concentration and low concentration group. The high concentration group includes 1,000 ppm, 500 ppm, 100 ppm, 50 ppm, 25 ppm and, 12.5 ppm. The low concentration group includes 6 ppm, 3 ppm, 1.5 ppm, 800 ppb, and 400 ppb. Figure 49 shows the concentration prediction results for 1.5 ppm when the trained data are low concentration samples and Figure 50 shows results for the 25 ppm when the trained data are high concentration samples. Figure 49 indicates that the trained model predicted the concentration of the tested solution within 0.9 – 1.2 ppm while the actual concentration is 1.5 ppm. However, in Figure 50, the model's prediction accuracy is very high as it is able to predict the concentration at around 25 ppm while the actual concentration of the tested solution is 25 ppm.

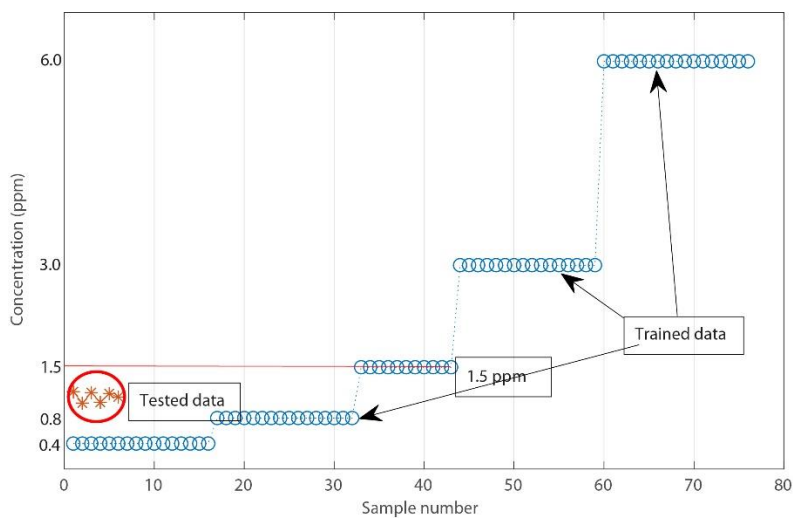


Figure 49. Concentration prediction of MgCl_2 salt solution (1.5 ppm).

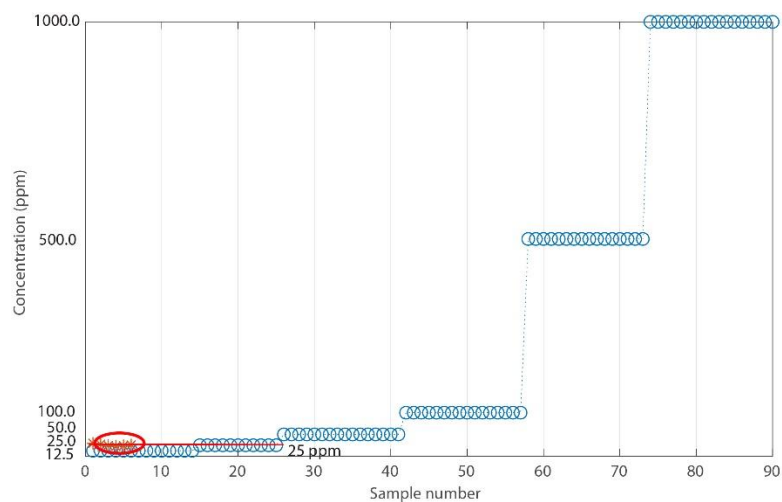


Figure 50. Concentration prediction of MgCl_2 salt solution (25.0 ppm).

In the appendix section, conductivity measurements for different concentrations of MgCl_2 salt solutions and standard deviation calculation for different concentrations of MgCl_2 solutions are presented.

5.5 Mix (NaCl and MgCl₂) solution results

In this project, we have performed an experiment with a mixture of two solutions. NaCl and MgCl₂ solutions are mixed together to prepare the mixed solutions. In chapter three, the detailed preparation process is presented for the mixed solution. Figure 51 shows the reflection coefficient (S_{11}) measurement for the mixed solution. We have prepared 100 ppm, 25 ppm, 6 ppm, 1.5 ppm and, 400 ppm concentrations of mixed solution to measure the reflection coefficient.

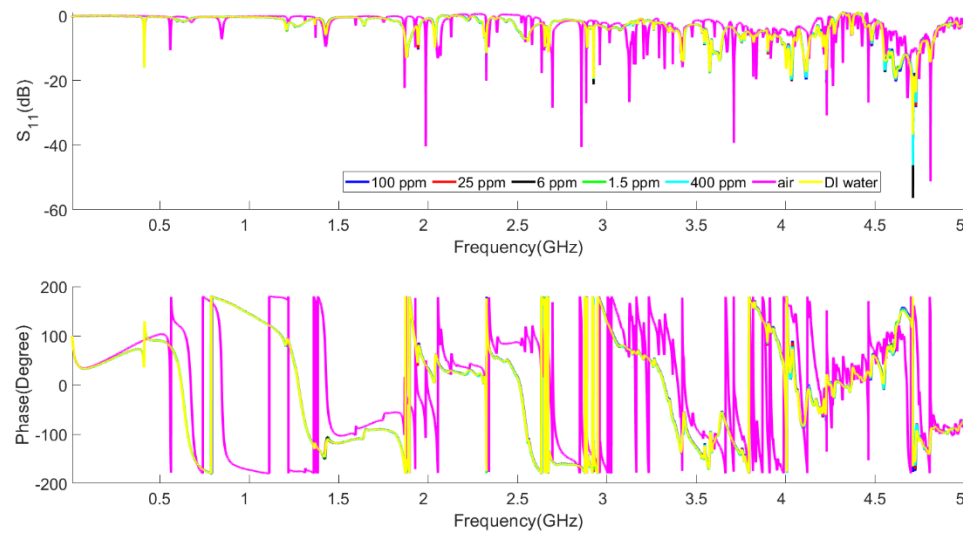


Figure 51. Reflection coefficient measurement of mixed solution (NaCl+ MgCl₂).

We have also applied the machine learning approach for the mixed solution. The trained data includes 100 ppm, 25 ppm, 6 ppm, 1.5 ppm and, 400 ppm. Figure 52 and Figure 53 present concentration prediction results of mixed solution for 1.5 ppm and 6.0 ppm respectively. The results indicate that the model prediction is very accurate for both 6 ppm and 1.5 ppm.

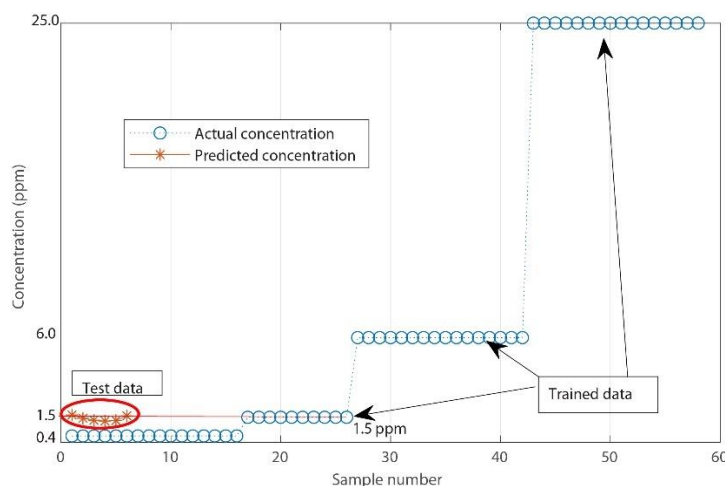


Figure 52. Concentration prediction of mix (NaCl+ MgCl₂) salt solution (1.5 ppm).

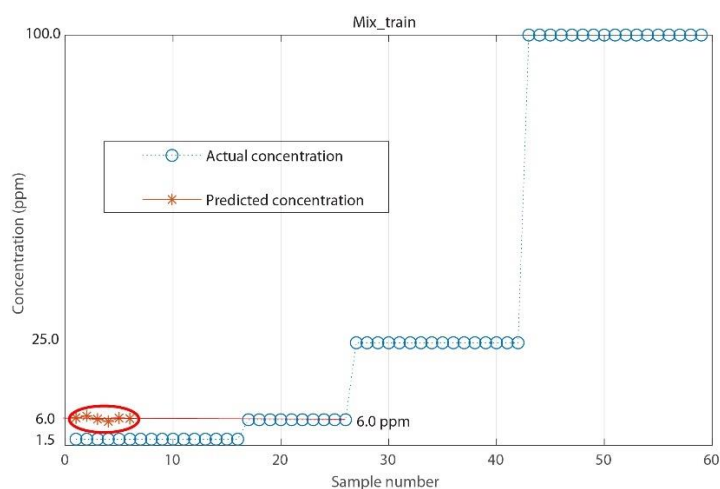


Figure 53. Concentration prediction of mix (NaCl+ MgCl₂) salt solution (6 ppm).

To test the feasibility of this sensor in identifying specific contaminants and their concentrations among multiple contaminated solutions, we tested with our mixed solutions (NaCl+ MgCl₂) with our separate NaCl and MgCl₂ solution. Figure 54 shows the reflection coefficient response for NaCl, MgCl₂ and mixed solution.

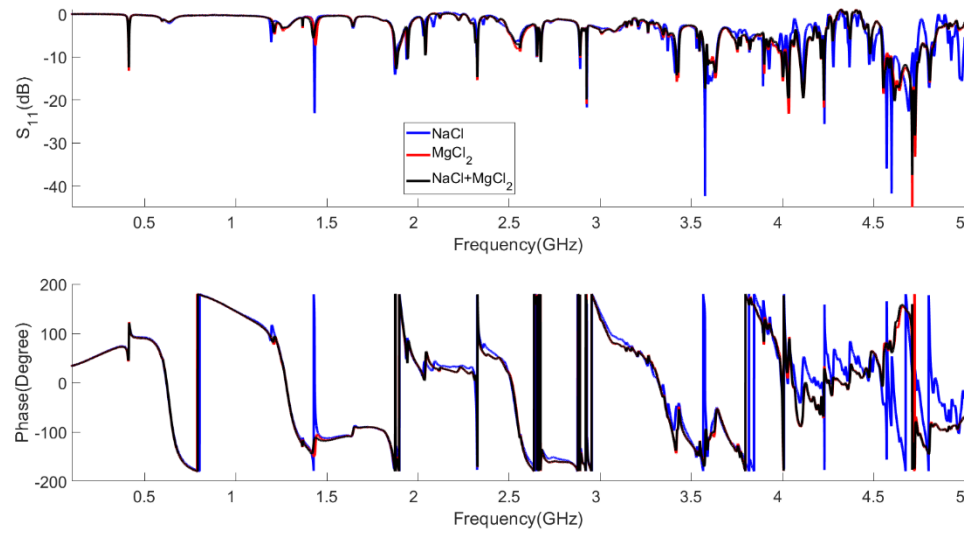


Figure 54. Reflection coefficient measurement for NaCl, MgCl₂, and mixture solutions.

We have also applied the machine learning approach for this experiment. For training the model, we used 100 ppm, 25 ppm, 6 ppm, 1.5 ppm, and 400 ppb solutions and tested with 100 ppm NaCl and 100 ppm MgCl₂ solution. Figure 55 and 56 shows the concentration prediction result for NaCl and MgCl₂ with 100 ppm concentration. The results indicate that the algorithm could not accurately predict the concentration of NaCl and the MgCl₂ solutions when multiple mixed concentrations are used to train the model.

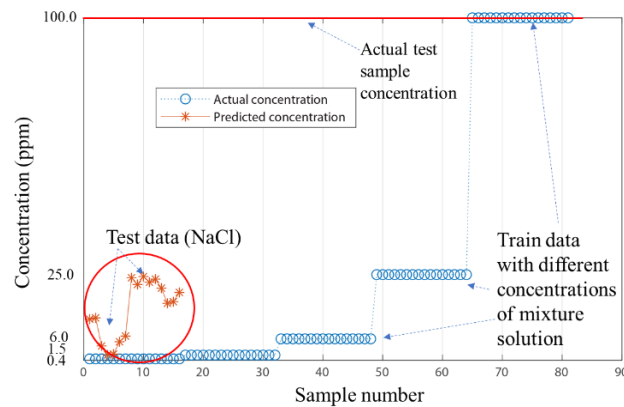


Figure 55. NaCl (100 ppm) concentration prediction test with different concentrations of mixed train data.

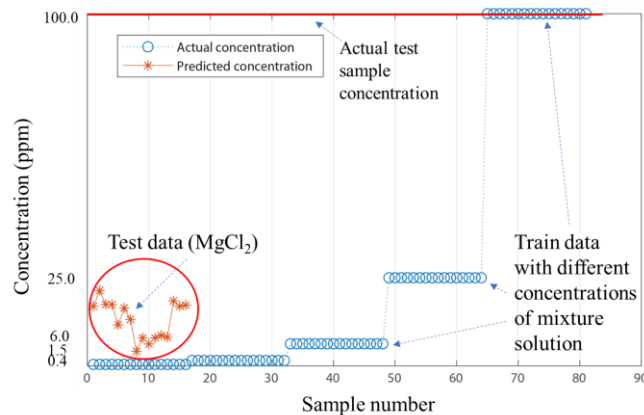


Figure 56. MgCl_2 (100 ppm) concentration prediction test with different concentrations of mix train data.

At the end of this results and discussion section, it can be proposed that the sensor's sensitivity is 400 ppb. The machine learning algorithm results indicate that the trained model can predict different concentrations with high precision when both the train and test data belong to the same materials solution. Improvement in data selection process and optimization of the algorithm is required to improve the SVR models prediction accuracy.

CHAPTER 6 CONCLUSION AND FUTURE WORK

6.1 Conclusion

A novel water contaminant detection method is presented in this thesis. This technology will allow us to measure specific water contaminants continuously in real-time. The sensor is mounted on the surface of a tube and the liquid sample is placed inside the tube. Reflection coefficient (S_{11}) is measured as a function of frequency and machine learning algorithm is applied to analyze the data. The SVR model is trained with the measured reflection coefficient data. The trained model predicts the concentration level of the liquid solution.

Experiments have been performed on sodium chloride (NaCl), magnesium chloride ($MgCl_2$) and the mixture of NaCl and $MgCl_2$. For NaCl and $MgCl_2$, 11 different concentrations of liquid solutions are tested. The results show that the algorithm can predict the concentration levels with high accuracy. From the experiments, it has been shown that the sensors can detect concentration level as low as 400 ppb. However, high sensitivity response is observed for concentration levels larger than 800 ppb. The experimental results indicate that this technology has significant potential to resolve the bottleneck problems of the existing water contaminant detection techniques.

6.2 Future work

The focus of this thesis was to develop a technology for water contaminant detection. Throughout the course of the investigation, the experiments were limited to

alkali and alkaline metal components. The development of this technology shows that we can apply this method for specific heavy metal (Pb) detection. To test the feasibility of this method for heavy metal detection, we prepared 5 different liquid samples of lead nitrate ($\text{Pb}(\text{NO}_3)_2$) salt solution and measured the reflection coefficient (S_{11}). Figure 57 shows the reflection coefficient result of $\text{Pb}(\text{NO}_3)_2$. Concentrations of the $\text{Pb}(\text{NO}_3)_2$ salt solutions at 5 ppm, 2.5 ppm, 1 ppm, 750 ppb, and 500 ppb.

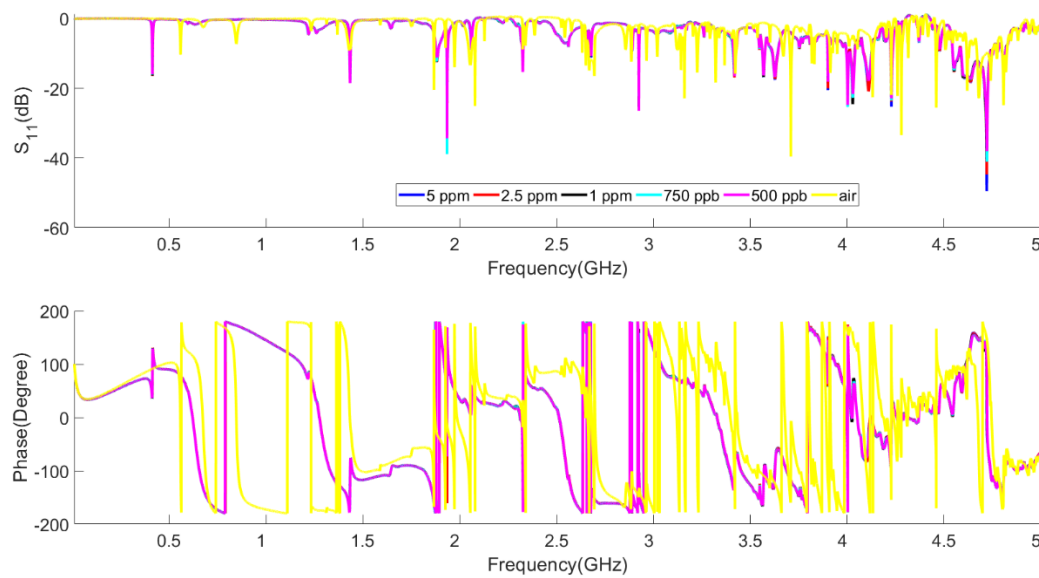


Figure 57. Reflection coefficient (S_{11}) response of $\text{Pb}(\text{NO}_3)_2$ from 10 MHz – 5.0 GHz.

Figure 58 shows the magnified response of reflection coefficient from 4.72 GHz – 4.74 GHz. The result indicates that with an increase in concentration, the amplitude of the reflection goes down. With an increase in concentration, more energy is absorbed. Thus, the reflected signal becomes weak and the amplitude value goes down.

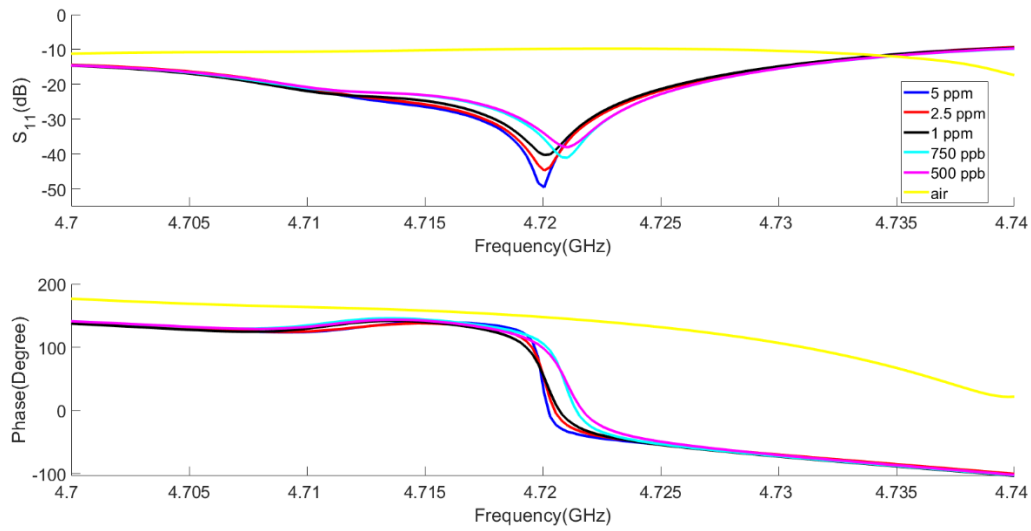


Figure 58. Reflection coefficient (S_{11}) response of $\text{Pb}(\text{NO}_3)_2$ from 4.72 GHz – 4.74 GHz.

The machine learning approach is also applied to predict the concentration level of the $\text{Pb}(\text{NO}_3)_2$ liquid solution. Figure 59 shows the test result for $\text{Pb}(\text{NO}_3)_2$ solution with 1 ppm concentration. The result indicates that the developed method can be applied for heavy metal detection. For the heavy metal solution, we experimented with concentrations as low as 500 ppb. However, the minimum detection limit for lead (Pb) as a heavy metal is 15 ppb [48]. Further optimization of the sensor is required to detect such a low concentration.

The algorithm needs to be optimized to predict the lower concentrations for lead solutions. Right now, the algorithm can not interpolate concentration levels between two given successive concentration level. A detailed understanding of which parameters are affecting the reflection coefficient response will help us to optimize the algorithm to determine the concentration level with a minimum percentage of error.

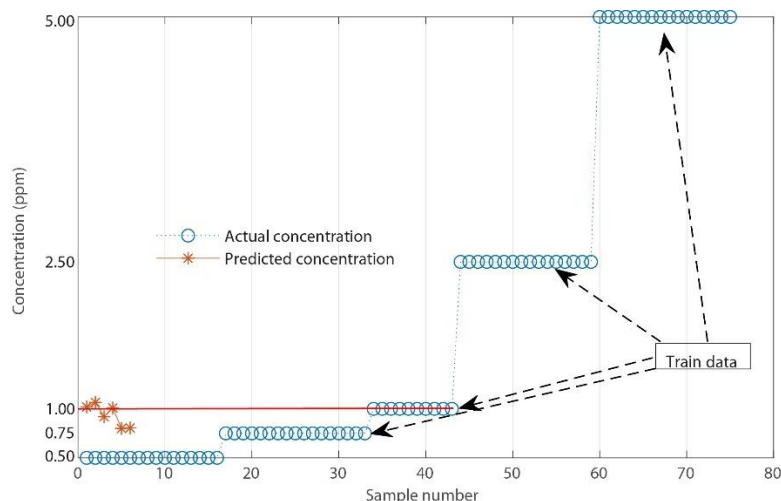


Figure 59. Concentration prediction of $\text{Pb}(\text{NO}_3)_2$ solution (1 ppm).

The cost of fabricating the sensor is less than \$1, but to measure the reflection coefficient, we are using a network analyzer, which is expensive. To reduce the cost of this technology we can apply the internet of things (IoT). Figure 60 shows a block diagram representation of the application of the IoT. The measured data from the test environment will be sent to the cloud. The electronics and high-speed computers with access to the cloud will be used to process the data (train and test) and the final result will be sent back to the display device. This process will allow us to apply the proposed contaminant detection technology to be used in remote areas as long as the internet connection is provided.

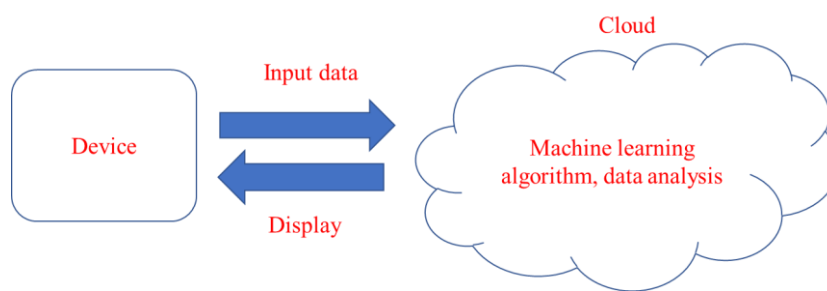


Figure 60. Internet of things (IoT).

CHAPTER 7 APPENDIX

7.1 Conductivity response of MgCl_2

Figure 61 shows the conductivity measurement result for MgCl_2 . The curve is shown linear characteristics until 12.5 ppm but for the lower concentrations (< 12.5 ppm), it does not follow the exact linear behavior.

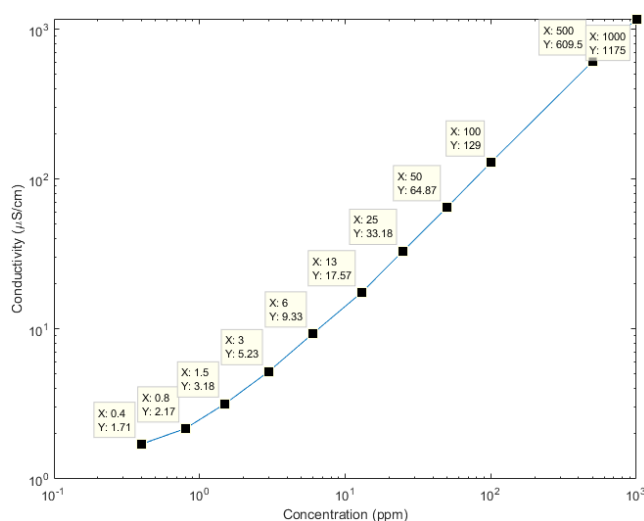


Figure 61. MgCl_2 conductivity measurement for different concentration solutions.

7.2 Standard deviation result for MgCl_2

Figure 62 represents the standard deviation for 11 different concentrations of MgCl_2 salt solutions. The graph indicates that the difference between different quartile with respect to the median is not equal for each concentration. The 100 ppm concentration solution has the most deviation and the 3 ppm concentration has the minimum deviation.

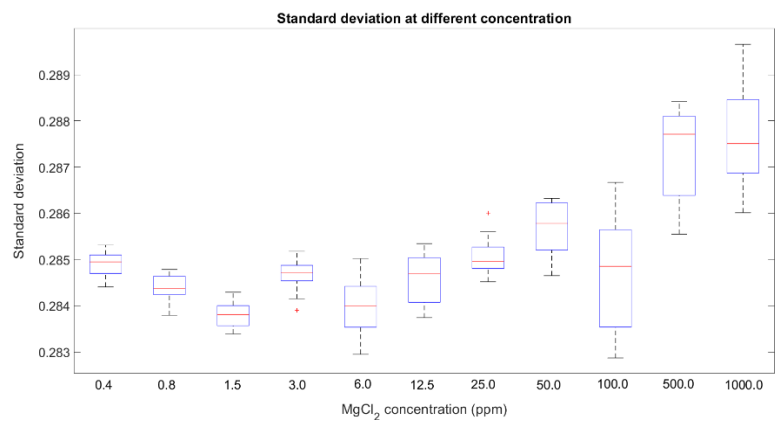


Figure 62. Standard deviation calculation for different concentration of MgCl₂ solutions.

BIBLIOGRAPHY

- [1] "Definition of "contaminant"," United States Environmental Protection Agency, [Online]. Available: <https://www.epa.gov/cccl/definition-contaminant>.
- [2] Yuncong Li, Kati Migliaccio, *Water Quality Concepts, Sampling and Analyses*, Boca Raton, FL: CRC Press, 2011.
- [3] Anderson, Don L., *Theory Of The Earth*, Blackwell Scientific Publications, 1989.
- [4] "Contaminant candidate list, regulatory determination support document for sodium," USEPA, Office of Water Report, July 2003.
- [5] "Drinking water advisory: Consumer acceptability advice and health effects analysis of sodium," February 2003. [Online]. Available: https://www.epa.gov/sites/production/files/2014-09/documents/support_cc1_sodium_dwreport.pdf. [Accessed February 2019].
- [6] "Normal physiology of sodium and potassium metabolism," in *Sodium-Restricted Diets and The Use of Diuretics: Rationale, Complications and Practical Aspects of Their Use*, 1979.
- [7] Dart, Richard C., *Medical Toxicology*, Philadelphia, 2004.
- [8] "Food, nutrition, physical activity, and the prevention of cancer: a global perspective," *World Cancer Research Fund, American Institute For Cancer Research*, 2007.
- [9] "Seawater," WIKIPEDIA, [Online]. Available: <https://en.wikipedia.org/wiki/Seawater>. [Accessed January 2019].
- [10] "How much sodium does a water softener put into your water?," Pure Water Products, LLC, 2019. [Online]. Available: <http://www.purewaterproducts.com/articles/sodium-in-soft-water>. [Accessed March 2019].
- [11] "Water softening," PennState Extension, 12 July 2011. [Online]. Available: <https://extension.psu.edu/water-softening>. [Accessed March 2019].
- [12] M. Legrand, M. de Angelis, R. J. Delmas, "Ion chromatographic determination of common ions at ultratrace levels in Antarctic snow and ice," *Analytica Chimica Acta*, vol. 156, pp. 181-192, 1984.
- [13] Susan D. Richardson, Thomas A. Ternes, "Water analysis: Emerging contaminants and current issues," *Analytical Chemistry*, vol. 90, pp. 398-428, 2017.
- [14] "Ion chromatography (IC)," Materials Evaluation and Engineering, Inc, 2019. [Online]. Available: <https://www.mee-inc.com/hamm/ion-chromatography-ic/>. [Accessed March 2019].

- [15] "Ion Chromatography Services," Process Sciences Incorporated, 2019. [Online]. Available: http://www.process-sciences.com/Ion_Chromatography_Services. [Accessed 30 April 2019].
- [16] Robert K. Boyd, Cecilia basic, Robert A. Bethem, Trace Quantitative Analysis by Mass Spectrometry, 2008.
- [17] Verdun, Alan G. Marshall, and Francis R., Fourier transforms in NMR, OPTICAL and MASS SPECTROMETRY, 1990.
- [18] J. Clark, "The Mass Spectrometer," Chemguide, March 2019. [Online]. Available: <https://www.chemguide.co.uk/analysis/masspec/howitworks.html>. [Accessed January 2019].
- [19] O. Menis, T.C. Rains, "Sensitivity, detection limit, precision and accuracy in flame emission and atomic absorption spectrometry," in *Analytical Flame Spectroscopy*, pp. 47-77.
- [20] Vijay Paul, Rakesh Pandey, Ramesh K.V. and R.C. Meena, "Atomic Absorption Spectroscopy (AAS) for Elemental Analysis of Plant Samples," *Manual of ICAR Sponsored Training Programme on "Physiological Techniques to Analyze the Impact of Climate Change on Crop Plants" 16-25 January, 2017, Division of Plant Physiology, IARI, New Delhi*.
- [21] Sanjida Afrin, M.Nuruzzaman Khan, Mohammed Mizanur Rahman, Papia Haque, "Determination of Serum Copper and Zinc Level of Bangladeshi Breast Cancer Patient," *ARC Journal of Cancer Science*, vol. 4, 2018.
- [22] Richard Wallace, Krister Andreasson, Introduction to RF and Microwave Passive Components, 2015.
- [23] "Inductive sensors," BALLUFF Inc, [Online]. Available: <https://www.balluff.com/local/us/products/sensors/inductive-sensors/>. [Accessed March 2019].
- [24] Norhisam Misron, Loo Qian Ying, Raja Nor Firdaus, Norrimah Abdullah, Nashiren Farzilah Mailah, Hiroyuki Wakiwaka, "Effect of inductive coil shape on sensing performance of linear displacement sensor using thin inductive coil and pattern guide," *Sensors*, vol. 11, no. 11, 2011.
- [25] Yehui Han, David J. Perreault, "Inductor design methods with low-permeability RF core materials," *IEEE Transactions on Industry Applications*, vol. 48, no. 5, 2012.
- [26] Wildi, Theodore, Electrical Machines, Drives and Power Systems, 2002.
- [27] B.L.Theraja, A.K. Theraja, A Textbook of Electrical Technology, Volume 1, Basic Electrical Engineering, New Delhi: S.Chand & Company Ltd., 1997.
- [28] Scott, Donald E., An Introduction to Circuit Analysis, McGraw-Hill Inc., 1987.
- [29] Bahl, Inder, Lumped Elements for RF and Microwave Circuits, London: Artech House, 2003.
- [30] Rizzi, Peter A., Microwave Engineering Passive Circuits, Prentice-Hall, Inc., 1988.

- [31] Ana Catarina Lopes, Ariane Sagasti, Andoni Lasheras, Virginia Muto, Jon Gutiérrez, Kouzoudis Dimitris and José Manuel Barandiarán, "Accurate Determination of the Q Quality Factor in Magnetoelastic Resonant Platforms for Advanced Biological Detection," *Sensors (Basel, Switzerland)*, vol. 18, 2018.
- [32] S. Kim, D.P. Neikirk, "Compact equivalent circuit model for the skin effect," *IEEE MTT-S International Microwave Symposium Digest*, 1996.
- [33] Pozar, David M., *Microwave Engineering*, Addison-Wesley Publishing company, Inc, 1990.
- [34] Network analyzer basics, keysight technologies, 2014.
- [35] Everette C. Burdette, Fred L. Cain, Joseph Seals, "In vivo probe measurement technique for determining dielectric properties at VHF through microwave frequencies," *IEEE Transactions on Microwave Theory and Techniques*, vol. 28, no. 4, 1980.
- [36] Ester C. F. A. Rosa, E. Capelas de Oliveira, "Relaxation equations: fractional models," *Journal of Physical Mathematics*, vol. 6, no. 2, 2015.
- [37] Balanis, Constantine A., *Advanced Engineering Electromagnetics*, John Wiley & Sons, Inc, 1989.
- [38] "Inductance," WIKIPEDIA, [Online]. Available: <https://en.wikipedia.org/wiki/Inductance>. [Accessed January 2019].
- [39] Knight, David W, "An introduction to the art of solenoid inductance calculation with emphasis on radio-frequency applications," 4 February 2016. [Online]. Available: <http://g3ynh.info/zdocs/magnetics/Solenoids.pdf>. [Accessed July 2018].
- [40] Knight, David W, "The self-resonance and self-capacitance of solenoid coils: applicable theory, models and calculation methods.," 4 May 2016. [Online]. Available: http://g3ynh.info/zdocs/magnetics/appendix/self_res/self-res.pdf. [Accessed July 2018].
- [41] M, Venkatesam, "Artificial intelligence vs. Machine learning vs. Deep learning," Data Science Central, 7 May 2018. [Online]. Available: <https://www.datasciencecentral.com/profiles/blogs/artificial-intelligence-vs-machine-learning-vs-deep-learning>. [Accessed March 2019].
- [42] Alex J. Smola, Bernhard Scholkopf, "A tutorial on support vector regression," *Statistics and Computing*, vol. 14, pp. 199-222, 2004.
- [43] Kotsiantis, S.B., "Supervised machine learning: a review of classification techniques," *Informatica*, vol. 31, pp. 249-268, 2007.
- [44] Reza Jalil Mozhdehi, Yevgeniy Reznichenko, Abubakar Siddique and Henry Medeiros, "Convolutional Adaptive Particle Filter With Multiple Models for Visual Tracking," in *13th International Symposium on Visual Computing*, Las Vegas, 2018.
- [45] Corinna Cortes, Vladimir Vapnik, "Support-Vector Networks," *Machine Learning*, vol. 20, pp. 273-297, 1995.

- [46] "fitrsvm," MathWorks, [Online]. Available:
<https://www.mathworks.com/help/stats/fitrsvm.html>. [Accessed february 2019].
- [47] "unwrap," MathWorks, [Online]. Available:
<https://www.mathworks.com/help/matlab/ref/unwrap.html>. [Accessed March 2019].
- [48] "Lead and Copper Rule: A Quick Reference Guide," [Online]. Available:
<https://nepis.epa.gov/Exe/ZyPDF.cgi?Dockkey=60001N8P.txt>. [Accessed 31 March 2019].